

# On the polar caps of the Three Musketeers<sup>1</sup>

A. De Luca, P. A. Caraveo, S. Mereghetti, M. Negroni<sup>1</sup>, G.F. Bignami<sup>1,2</sup>

*Istituto di Astrofisica Spaziale e Fisica Cosmica,  
Sezione di Milano “G. Occhialini” - INAF  
v. Bassini 15, I-20133 Milano, Italy*

deluca@mi.iasf.cnr.it

## ABSTRACT

XMM-Newton observations of PSR B0656+14, PSR B1055-52 and Geminga have substantially increased the statistics available for these three isolated neutron stars, so apparently similar to deserve the nickname of “Three Musketeers” (Becker & Trümper, 1997). Here we shall take advantage of the EPIC statistics to perform phase resolved spectroscopy for all three objects. The phase-averaged spectrum of the three musketeers is best described by a three component model. This includes two blackbody components, a cooler one, possibly originating from the bulk of the star surface, and a hotter one, coming from a smaller portion of the star surface (a “hot spot”), plus a power law. The relative contributions of the three components are seen to vary as a function of phase, as the stars’ rotation bring into view different emitting regions. The hot spots, which have very different apparent dimensions (in spite of the similarity of the three neutron stars polar cap radii) are responsible for the bulk of the phase variation. The amplitude of the observed phase modulation is also markedly different for the three sources. Another striking aspect of our phase-resolved phenomenology is the apparent lack of any common phase alignment between the observed modulation patterns for the two blackbody components. They are seen to vary *in phase* in the case of PSR B1055-52, but *in anti-phase* in the case of PSR B0656+14. These findings do not support standard and simplistic models of neutron star magnetic field configuration and surface temperature distribution.

---

<sup>1</sup>Università degli Studi di Pavia, Dipartimento di Fisica Nucleare e Teorica, Via Bassi 6, 27100 Pavia, Italy

<sup>2</sup>Centre d’etude spatiale des Rayonnements, CNRS-UPS, 9, Avenue du Colonel Roche, 31028 Toulouse Cedex 4, France

*Subject headings:* pulsars: general — pulsars: individual (Geminga, PSR B0656+14, PSR B1055-52) — stars: neutron — x-ray:stars

## 1. Introduction

PSR B0656+14, PSR B1055-52 and Geminga are isolated neutron stars showing similar periods and period derivative. Hence their characteristic ages (few 100 thousand years), their inferred magnetic fields (few  $10^{12}$  G) and their energetics ( $\dot{E}_{rot} \sim 10^{34}$  erg s $^{-1}$ ) are very similar. Moreover, they are all nearby, making it easier to detect them at different wavelengths. Parallax distance measurements are available for Geminga (157 pc, Caraveo et al., 1996) and PSR B0656+14 (288 pc, Brisken et al., 2003), while for PSR B1055-52 the current distance estimate, based on the dispersion measure, is  $\sim 750$  pc (Kramer et al., 2003). In X-rays they shine both owing to thermal and non-thermal mechanisms. Blackbody emission, from the majority of their surface, is seen to be complemented at higher energies by power law “tails”. They have faint optical counterparts, with visual magnitude  $m_v \sim 25.5$  for Geminga (Bignami et al., 1987),  $\sim 25$  for PSR B0656+14 (Caraveo et al., 1994) and  $\sim 24.9$  for PSR B1055-52 (Mignani et al., 1997). Multicolor photometry, available for Geminga and PSR B0656+14, shows that their NUV magnitudes are broadly compatible with the extrapolations of their X-ray blackbody emissions, while a power law-like excess is apparent in the optical/NIR (Mignani et al., 2004 and references therein). While PSR B1055-52 and Geminga are bona fide gamma-ray pulsars (Fierro et al., 1993; Bertsch et al., 1992), for PSR B0656+14 a tentative detection awaits confirmation (Ramanamurthy et al., 1996).

Here we shall concentrate on the analysis of the XMM-Newton data collected both in imaging and timing mode. Such exceptional harvest of X-ray photons over the ample energy interval covered by the EPIC cameras allows us to use a new tool for the study of the X-ray behaviour of the “Three musketeers”: phase resolved spectroscopy.

While we have already published the phase-resolved analysis of the EPIC/pn data on Geminga (Caraveo et al. 2004), here we shall include also this source, in order to underline similarities and differences in the phase resolved X-ray behaviour of three otherwise very similar objects.

---

<sup>1</sup>Based on observations with XMM-Newton, an ESA science mission with instruments and contributions directly funded by ESA member states and the USA (NASA).

## 1.1. Review of the X-ray observations of the Three Musketeers

The EPIC data presented below come after two decades of X-ray observations of isolated neutron stars, starting with their discovery as soft, probably thermal sources by the Einstein Observatory.

### 1.1.1. Geminga

1E 0630+178 was discovered by the Einstein satellite while covering the gamma-ray error box of the unidentified source Geminga (Bignami et al., 1983). The discovery of a common 237 msec pulsation clicked the identification, the first ever, of an unidentified gamma-ray source with its X-ray counterpart (Halpern & Holt, 1992; Bertsch et al., 1992). The first good quality spectral data on Geminga were collected by ROSAT. Halpern and Ruderman (1993), using 7,911 photons in the 0.07-1.50 keV energy band, concluded that the spectrum was well described by two black-body curves at temperatures of  $0.5 \times 10^6$  K and  $3 \times 10^6$  K. While the cooler component appeared to come from the full surface of the neutron star, the hotter one could have been coming from a spot covering just  $3 \times 10^{-5}$  of the neutron star surface, possibly due to a heated polar cap. A second, longer ROSAT observation, yielding 18,500 soft photons, was analysed together with an observation by ASCA, providing the first 1,750 “hard” ( $> 2$  keV) counts. Such a combination seemed to favour a different, composite interpretation, where, a power-law, non-thermal emission was added to the low temperature black-body radiation (Halpern and Wang, 1997). The power-law photon index was still poorly constrained, ranging from 2.2 to 1.5. Using a longer ASCA observation with 4,800 photons, Jackson et al. (2002) confirmed the composite nature of Geminga’s spectrum and refined the power-law photon index value to  $1.72 \pm 0.1$ . They tried also to perform some phase-resolved spectroscopy, but could only use two phase intervals. They found the spectrum of the interval including the peak to be slightly softer than the rest of the light curve, but concluded that “the difference is only marginally significant”.

### 1.1.2. PSR B0656+14

The definitely brighter PSR 0656+14 was first detected by the Einstein satellite (Cordova et al., 1989). A ROSAT PSPC observation allowed Finley et al. (1992) to detect the X-ray pulsation and to measure a pulsed fraction of  $14\% \pm 2\%$ . Further pointings were then carried out with the ROSAT PSPC detector in 1992 (Oegelman, 1995), for a total exposure time of about 17 ksec, collecting  $\sim 32,000$  photons in the 0.1-2.4 keV band. The

overall ROSAT dataset was analyzed by Possenti et al. (1996), who found the bulk of the emission to be of thermal origin, well described by a blackbody curve ( $T \sim 9 \times 10^5$  K) originating from a large part the star surface (emitting radius  $\sim 14$  km, assuming a distance of 760 pc, corresponding to  $\sim 5.3$  km at the parallactic distance of 288 pc). A second spectral component was required to describe the higher energy part of the spectrum, as well as to explain a significant change of the pulse profile with energy. It was not possible however to discriminate between a second blackbody component ( $T \sim 1.9 \times 10^6$  K) originating from a region a few hundred times smaller and a steep ( $\Gamma \sim 4.5$ ) power law. Greiveldinger et al. (1996) coupled the ROSAT dataset to an ASCA observation which yielded  $\sim 2,000$  photons in the 0.5-10 keV band. Their best fit used a three component model: the sum of two blackbodies (best fit parameters very similar to the results of Possenti et al. 1996) and of a power law with photon index  $\Gamma = 1.5 \pm 1.1$ . More recently, PSR B0656+14 was observed with Chandra, both with ACIS and with the LETG. The ACIS data ( $\sim 45,000$  photons in the 0.2-6 keV range) confirmed a three-component model to yield the best description of the spectrum (Pavlov et al., 2002), consistent of the sum of two blackbodies ( $T_1 \sim 0.85 \times 10^6$  K,  $R_1 \sim 12$  km;  $T_2 \sim 1.65 \times 10^6$  K,  $R_2 \sim 1$  km, using a distance of 500 pc; assuming the distance of 288 pc,  $R_1 \sim 7$  km and  $R_2 \sim 0.6$  km). The high spectral resolution of the Gratings allowed Marshall & Schultz (2002) to exclude the presence of significant features superimposed on the thermal continuum in the softer band (0.15-1 keV). The parameters of their best fitting two-blackbody model are  $T_1 \sim 0.8 \times 10^6$  K,  $R_1 \sim 22.5$  km;  $T_2 \sim 1.5 \times 10^6$  K,  $R_2 \sim 1.7$  km, assuming a distance of 760 pc, corresponding to  $R_1 \sim 8.5$  km and  $R_2 \sim 650$  m at the distance of 288 pc.

### 1.1.3. PSR B1055-52

After the Einstein observatory discovery of X-ray emission from this radio pulsar (Cheng & Helfand, 1983), PSR B1055-52 was observed with ROSAT, both with the HRI (8.6 ksec yielding  $\sim 570$  source photons) and with the PSPC (15.6 ksec, for a total of  $\sim 5500$  source photons) in 1990-1992 (Oegelman & Finley, 1993). The timing analysis unveiled the source pulsation, with a pulsed fraction increasing from  $\sim 11\%$  for energies  $< 0.5$  keV to  $\sim 63\%$  above 0.5 keV. The spectrum was best described by a two component model. A blackbody with temperature of  $\sim 8 \times 10^5$  K, coming from a large portion of the surface, accounts for the bulk of the X-ray emission; a second component was required, either a second, hotter ( $T \sim 3.6 \times 10^6$  K) blackbody coming from an area a few  $10^4$  times smaller, or a steep ( $\Gamma \sim 4$ ) power law. An ASCA observation could add only  $\sim 200$  photons in the 0.5-10 keV range (Greiveldinger et al., 1996). A Chandra ACIS observation was taken in 2000 (42 ksec exposure); results were summarized by Pavlov et al. (2002). A simultaneous fit to Chandra and ROSAT data

required a three component model, consisting of the sum of two blackbodies ( $T_1 \sim 8.3 \times 10^5$  K,  $R_1 \sim 12$  km;  $kT_2 \sim 1.6 \times 10^6$  K,  $R_2 \sim 800$  m assuming the distance to be 1 kpc;  $R_1 \sim 9$  km,  $R_2 \sim 600$  m at the revised distance of 750 pc) and of a power law ( $\Gamma \sim 1.7$ ). The above authors reported the presence of a significant variation of the hot blackbody component, observed through phase-resolved spectroscopy, but they did not present detailed results. A similar three component model has been used by Becker & Aschenbach (2002) in their analysis of XMM-Newton data. Spectroscopy was performed using MOS data only, which were fitted together with ROSAT data. Their best fit was obtained with  $T_1 \sim 7.1 \times 10^5$  K,  $R_1 \sim 31$  km,  $T_2 \sim 1.4 \times 10^6$  K,  $R_2 \sim 2.6$  km assuming the distance to be 1 kpc (at the revised distance of 750 pc the emitting radii are  $R_1 \sim 15.5$  km,  $R_2 \sim 1.3$  km); the power law photon index was found to be  $1.9 \pm 0.2$  and the interstellar absorption  $N_H \sim 2.3 \times 10^{20} \text{ cm}^{-2}$ .

## 2. The XMM-Newton/EPIC data sets

Geminga, PSR B0656+14 and PSR B1055-52 were observed by XMM-Newton as Guaranteed Time targets. The complete journal of observations is reported in Table 1. The data are now available in the XMM-Newton Science Archive.

While the MOS cameras (Turner et al., 2001) were operated in Full Frame mode in order to image on the full field of view of the telescopes (15' radius), the pn detector (Strüder et al., 2001) was used to time-tag the photons, either in Small Window mode (6 ms time resolution, imaging on a  $4' \times 4'$  field) or in Fast Timing Mode (0.03 ms resolution, no spatial information along detector columns). Unfortunately, as pointed out by Becker & Aschenbach (2002), the use of the potentially promising Fast Timing mode produces, as a byproduct, a background significantly higher than in Small Window mode, owing to the peculiar readout mode and to the collapse of data along the CCD columns. Such an abnormally high background lowers the signal-to-noise above a few keV.

### 2.1. Data reduction and background screening

All the data reduction was performed using the most recent release of XMM-Newton Science Analysis Software (SASv6.0.0). The raw Observation Data Files (ODFs) were processed using standard pipeline tasks (*epproc* for pn, *emproc* for MOS data). We selected events with PATTERN 0-4 and PATTERN 0-12 for the pn and the MOS, respectively.

Particular care was devoted to reduce the instrumental background in the linearized event lists. First, an accurate screening for soft proton flare events was done, following

the prescription of De Luca & Molendi (2004). We computed Good Time Intervals (GTIs) setting a threshold of  $3\sigma$  from the quiescent rate on the 0.5-12 keV count rate for both the pn and the MOS detectors. A more stringent threshold was adopted in the case of pn Fast Timing mode observations, since the collapse of data along the CCD readout direction increases (by a factor  $\sim 30$ ) the background count rate in the source extraction region.

The pn Fast Timing mode data required a further cleaning. Such operating mode is affected by a peculiar flaring background component (“Soft Flares”, see Burwitz et al., 2004) ultimately due to the interaction of charged particles (possibly heavy ions) with the CCD. Such interactions produce short (0.1-0.5 s time scale) and very intense bursts of events, with typical energies of  $\sim 0.22$  keV for singles (mono-pixel events) and of  $\sim 0.45$  keV for doubles (bi-pixel events). To remove such background noise, which would hamper the study of the low-energy emission of our targets, ad-hoc GTI files for singles and doubles were created, extracting 1-sec binned light curves in the 0.2-0.3 keV and 0.4-0.5 keV energy ranges, respectively, and then using the same algorithm adopted for the soft proton case.

The overall GTI filter for each pn Fast Timing observation was then obtained by intersecting the soft proton GTI, the soft flares GTI for singles and the soft flares GTI for doubles. The net exposure times (after dead-time correction) for the cleaned event lists are reported in Table 1. In the case of PSR B1055-52 the observation was splitted between two XMM revolutions (186 and 187). Event lists obtained with the same instrument in the same mode in different orbits were then merged using the SAS task *merge*.

## 2.2. Source and background events selection

To extract the source photons from the dataset taken in imaging modes (Full Frame for MOS and Small Window for pn) we selected a circle of  $45''$  radius, containing  $\sim 90\%$  of the counts; in Fast Timing mode we used a 17 pixel wide strip ( $4.1''$  pixel size), containing  $\sim 85\%$  of the source counts. Background photons were extracted from suitable regions on the same CCD chip containing the source: for Full Frame MOS images we need an annulus of  $2'$  inner radius and  $4'$  outer radius; for the pn detector operated in small window we selected two rectangular regions oriented along the CCD readout direction and covering  $\sim 2$  square arcmin; for pn used in Fast Timing mode we selected two stripes (17 and 12 pixels wide) away from the source region.

The 0.25-8.0 keV count rate observed in MOS1 camera for PSR B0656+14 is of  $\sim 0.9$  counts  $s^{-1}$ . A modest pile-up is expected, owing to the slow CCD readout in the Full Frame mode (2.6 sec frame time). An analysis of the event PATTERN distribution, performed with

the SAS task *epatplot*, clearly showed such effect as an excess of bi-pixel events above 0.7 keV. To solve the problem, we simply excluded the PSF core (inner 5", containing about 35% of the source photons), where the pile up could be significant. No hints for pile-up in the resulting photon list was apparent in the corresponding event PATTERN distribution.

In the case of PSR B1055-52, EPIC MOS images show a faint source at an angular distance of 32" in the NE direction (see Figure 17 of Becker & Aschenbach, 2002). Such source has a hard spectrum (possibly a background AGN); its flux, negligible wrt. the pulsar below 2 keV, becomes comparable to the pulsar's one above 3 keV. In order to avoid possible contaminations in the study of the pulsar high energy emission we decided to exclude such source from the pulsar extraction region, using a 10" arcsec radius circle (containing  $\sim 60\%$  of the counts at 5 keV) as a geometrical mask. Such a selection was not possible in pn Timing mode, since along the RAWX direction (perpendicular to the readout direction), where spatial information is maintained, the angular separation of the two sources is  $<4$  pixels. Therefore, the flux measured by the pn above  $\sim 3$  keV is possibly contaminated by some contribution from such background source and its absolute value should be taken with caution.

Background-subtracted count rates for the three neutron stars are reported in Table 1, together with the number of collected photons.

### 3. EPIC Data analysis

With a number of time-tagged photons (see Table 1) more than doubling all previous statistics, EPIC offers now the first chance of meaningful phase-resolved spectroscopy for the three musketeers.

Following the procedure outlined by Caraveo et al. (2004):

- first, we address the phase averaged spectral shape of the three objects to obtain useful pieces of information on the components needed to fit their overall spectra;
- next, we perform the timing analysis to search for the best period and to perform the phase alignment;
- then, we divide the folded light-curves in 10 phase intervals and extract the spectra corresponding to each phase interval;
- finally, each spectrum is fitted using the same components found to best describe the integrated spectrum and the corresponding phase-resolved spectral parameters are

computed.

In the following section we will discuss in detail each step for the cases of PSR B0656+14 and PSR B1055-52. The case of Geminga was described by Caraveo et al.(2004); we will report here the results to ease a synoptic view of the phenomenology of the three musketeers.

### 3.1. Phase-integrated spectral analysis

Spectra for the source and background events, extracted using the regions described in Sect. 2.2, were rebinned in order to have at least 40 counts/channel. We added a 5% systematic error to each spectral bin, to account for calibration uncertainties among different instruments/modes. *Ad hoc* redistribution matrices and effective area files were generated using the *rmfgen* and *arfgen* tasks of the SAS. The spectral analysis was performed with XSPEC v11.2. We selected 0.25 keV as lower bound for the spectral study, since below such an energy the calibration is still uncertain; the upper bound was selected on the basis of the observed signal-to-noise, which depends both on the sources' spectra and on the operating mode used. As discussed in Sect. 2.1, the spectra collected by the pn in Fast Timing mode suffer from a rather high background, which hampers the study of our targets at high energy, where such sources are rather faint. For PSR B0656+14 spectra obtained in Fast Timing mode turned out to be useful up to 2 keV, while for PSR B1055-52 we could include data up to 6 keV. Spectra from MOS1/2 Full Frame mode, as well as from pn sw mode, were used up to 8 keV. MOS and pn spectra were fitted simultaneously, leaving a cross-normalization factor as the only free parameter.

No significant spectral features are detected superimposed on the continuum of the three musketeers, neither in emission nor in absorption. As in the case of Geminga (Caraveo et al., 2004) (Fig.1), the best fitting model is found combining two blackbody curves and a power law. This confirms the findings of Pavlov et al. (2002), based on Chandra observations of PSR B0656+14 and PSR B1055-52, and Becker & Aschenbach (2002), who analyzed XMM-Newton (MOS only) data for PSR B1055-52. Using the best fitting parameters reported in Table 3 we obtain  $\chi^2_\nu=1.1$  (368 d.o.f.) for PSR B0656+14 (Fig.2) and  $\chi^2_\nu=1.0$  (327 d.o.f.) for PSR B1055-52 (Fig.3). The use of a second power law instead of the hotter blackbody yields photon indices of  $\sim 6.5$  for PSR B0656+14 and  $\sim 5.6$  for PSR B1055-52, while lowering the fit quality ( $\chi^2_\nu > 1.5$  and  $\chi^2_\nu > 1.1$  for the two cases, respectively). We note that a single-temperature, magnetized neutron star atmosphere model (Zavlin et al. 1996) cannot adequately reproduce the profile of the low-energy part of the spectrum of PSR B0656+14 and PSR B1055-52, similarly to the case of a single blackbody curve. Moreover, such model requires a very large emitting surface (with emitting radii of  $\sim 100$  km - this is true also for



Geminga). Therefore such model cannot provide a satisfactory description of the spectra of the three musketeers.

A synoptic plot of the spectra of the three musketeers is shown in Fig. 4. It is easy to note the definitely higher signal to noise in the high energy portion ( $>2$  keV) of the spectrum of Geminga, in spite of a flux only slightly higher in such energy range. This is mainly due to the different operating modes used for the pn detector in the observations of the three targets, especially to the much lower background in the pn small window mode wrt. Fast timing mode. The power law component in the spectra of PSR B0656+14 and PSR B1055-52 is constrained by the MOS spectra and (in the case of PSR B0656+14) by the short pn small window observation (see the caption to Fig. 4 for further details). We summarize the results of the EPIC spectral fits for the three musketeers in Table 3, where errors are computed at 90% confidence level for a single interesting parameter. The lower temperature blackbody (hereafter “cool blackbody”) is associated to an emitting region with an area compatible with the full surface of the neutron star. The higher temperature component (“hot blackbody”) is seen to originate from a much smaller area. To visualize the correlation between different spectral parameters we computed confidence contours (at 68%, 90% and 99% levels for two parameters of interest) for the interstellar column density  $N_H$  vs. the cool blackbody emitting area; this is shown in the insets in Fig. 1, Fig. 2 and Fig. 3.

As shown in Fig. 4, the overall shape of the spectrum of the three musketeers is very similar. However remarkable differences in the luminosity of different spectral components are immediately evident (see Table 3). In particular, we note that the luminosity of the hot blackbody in the case of Geminga is  $\sim 2$  orders of magnitude lower than in the other two cases. At variance with PSR B0656+14 and PSR B1055-52, for Geminga the contribution of the power law dominates over the hot blackbody in the energy range where the hot blackbody has its maximum.

The parameters best fitting the EPIC spectrum of PSR B1055-52 (see Table 3) are fully consistent with the results reported by Becker & Aschenbach (2002) and by Pavlov et al.(2002), who included ROSAT data in their spectral fits to EPIC/MOS and Chandra/ACIS data, respectively. The same is true in the case of Geminga: although we use a 3 component model, the results for the Cool blackbody component (temperature and emitting radius) are found to be very similar to the ROSAT ones (see e.g. Halpern & Ruderman, 1993). The case of PSR B0656+14 is slightly different: the interstellar column density ( $4.3 \pm 0.2 \times 10^{20}$  cm $^{-2}$ ) resulting from the symultaneous fit to the pn/Fast Timing, pn/Small Window and MOS1/Full Frame data is larger than the values ( $\sim 2 \times 10^{20}$  cm $^{-2}$ ) obtained by Pavlov et al.(2002) and Marshall & Schulz (2002) (based on Chandra ACIS/LETG data) and by Possenti et al.(1996) (based on ROSAT data). Thus, our analysis of the EPIC data results

in a brighter underlying continuum at low energies, leading to a lower temperature coupled to a larger emitting surface for PSR B0656+14. Addressing such a discrepancy, possibly due to subtle cross-calibration issues, is beyond the scope of our fitting exercise, which was performed to provide the starting point for the phase-resolved spectroscopy of the EPIC data.

### 3.2. Timing analysis

As a first step, we have studied the high time resolution pn data in order to derive the period of our targets. Source photons were selected from the regions described above, in the energy range 0.15-8 keV for pn Small Window mode and 0.15-2 keV for pn Fast Timing mode<sup>2</sup>. Photon time of arrivals were converted to the Solar System barycenter using the SAS task *barycen* and folded using 10 bins in a range of trial periods around the expected values. A very significant detection of the pulsation was obtained in each case. To determine with higher accuracy the period value and to evaluate the corresponding error, we followed the prescription of Leahy (1987).

The results are reported in Table 2, where they are compared with the extrapolations of the radio ephemeris, selected to be the nearest to the XMM-Newton observation. The period for the radio-quiet Geminga is compared to the  $\gamma$ -ray ephemeris of Jackson et al. (2002), based on the analysis of the complete EGRET dataset. A perfect consistency between the expected and measured values is apparent.

In order to align in phase the X-ray light curves with the radio (or gamma) ones, we have folded XMM-Newton data using the radio timing solutions for PSR B0656+14 and PSR B1055-52 and the gamma one for Geminga. The absolute accuracy of the XMM-Newton clock is  $\sim 500 \mu s$ , as stated by the calibration team (Kirsch, 2004) and by recent investigations (e.g. Becker et al., 2004). The extrapolation of the radio ephemeris to the time of the XMM observations yields a phase uncertainty of  $\sim 0.01$  for PSR B0656+14 (corresponding to 1/5 of phase bin in Fig. 5) and of  $\sim 0.003$  (1/20 of phase bin in Fig. 5) for PSR B1055-52, for which the clock accuracy is the dominant factor, since the radio data are almost simultaneous to the X-ray ones.

A larger uncertainty,  $\sim 0.15$  in phase, is present in the case of Geminga, as discussed by Caraveo et al. (2004), owing to the much longer time separation between the EGRET

---

<sup>2</sup>Time-tagging of photons is reliable over the whole detector sensitivity range; therefore we include in the timing analysis also low energy ( $E < 0.25$  keV) photons, not used for spectroscopy (see Sect.3.1)

and XMM-Newton observations.

The folded pulse profiles (background-subtracted) of our targets using the overall EPIC energy range are shown in Fig. 5. To ease their comparison, all the lightcurves have been plotted setting phase 0 to the X-ray pulse maximum as seen in the overall energy band. The phases of the radio peaks (PSR B0656+14 and PSR B1055-52) and  $\gamma$ -ray peaks (Geminga and PSR B1055-52) are also shown. Pulsed fractions have been computed as the ratio between the counts above the minimum and the total number of counts, deriving the corresponding uncertainties from the propagation of the statistical errors in the folded light curves.

We have then studied the variations of the pulse profiles with energy. The light curves relative to four energy intervals are shown in Fig. 6 (PSR B0656+14), Fig 7 (PSR B1055-52) and Fig. 8 (Geminga). Note that the energy ranges used are different for different targets, since for each source the energy intervals have been chosen in order to visualize the light curve relative to the cool blackbody, transition region, hot blackbody and power law. The lower panels of figures 6 and 7 show the radio profile of PSR B0656+14 and PSR B1055-52 at 0.67 GHz<sup>3</sup>. For the case of Geminga (Fig. 8), the  $\gamma$ -ray light curve<sup>4</sup> is shown. Ten phase intervals, selected *a priori*, to be used for phase-resolved spectroscopy (see Sect. 3.3) are marked in the upper panel. Our three neutron stars exhibit vastly different phenomenologies. The main results may be summarized as follows (see also the captions to Fig. 6, Fig 7 and Fig. 8):

- For PSR B0656+14 a single pulse per period may be seen in each energy band. The pulse shape below 1.5 keV is broadly sinusoidal; a significant change in pulse profile occurs between the energy range dominated by the cool blackbody and the range dominated by the hot blackbody. As a consequence, in the intermediate range the pulsed fraction reaches its minimum value. At higher energy, the pulse profile seems sharper, although the low statistics does not allow to study its shape (nor the pulsed fraction) with great accuracy. Note that the light curve above 1.5 keV was obtained by folding data from the short pn Small Window mode observation; the other cases represent data from the longer Fast Timing observation. Considering the overall light curve (Fig. 5), the single radio peak lags the X-ray maximum by  $\sim 0.25 \pm 0.05$  in phase (the uncertainty is dominated by the X-ray light curve bin width for the determination of the position of the X-ray peak), occurring very close to the X-ray minimum. In the

---

<sup>3</sup>Retrieved from the European Pulsar Network database, <http://www.mpifr.bonn.mpg.de/div/pulsar/data/browser.html>

<sup>4</sup>this was obtained by selecting 9 EGRET Viewing periods in which the target was imaged close to the center of the field of view and having a good photon statistics; events with energy  $E > 100$  MeV were extracted from the source position; time of arrivals were converted to the solar system barycenter and folded with the ephemeris published by Jackson et al. (2002)

lower panel of Fig. 6 we mark the phases of the double-peaked pulse profile observed in the V band by Kern et al.(2003). The position of the single  $\gamma$ -ray peak claimed by Ramanamurthy et al.(1996) is also indicated.

- Also PSR B1055-52 shows a single pulse per period at all energies, with a markedly different shape in the softest band (below 0.35 keV) wrt. intermediate energy ranges (0.35-1.5 keV), while above 1.5 keV the low signal-to-noise hampers the study of the pulse profile. The pulsed fraction, which is seen to grow with energy, is remarkably high ( $\sim 70\%$ ) in the band where the hot blackbody dominates the neutron star emission. The two peaks of the radio profile are seen to contour the X-ray peak at all energies; in the overall light curve the highest radio peak lags the X-ray one by  $\sim 0.2 \pm 0.05$  (the uncertainty is dominated by the X-ray light curve binning). The phase interval where the  $\gamma$ -ray pulse occurs lies between the X-ray maximum and the highest radio peak.
- Geminga shows a different behaviour of the pulse shape as a function of energy. The single, broad peak seen at low energy, where the cool blackbody dominates, changes to a double peak towards higher energies, where the bulk of the emission is non-thermal (power law component). The pulsed fraction reaches a maximum of  $>50\%$  in the energy range where the hot blackbody is more important. The significant uncertainty ( $\sim 0.15$ ) affecting the extrapolation of the EGRET ephemeris (see above) prevents any firm conclusion on the alignment between the X-ray and the  $\gamma$ -ray light curves.

### 3.3. Phase-resolved spectroscopy

The results of the spectral and timing analysis were then used to study the variation of the emission spectrum with pulse phase. For both PSR B0656+14 and PSR B1055-52 we selected photons whose times of arrival fall into the 10 different phase intervals marked on Fig. 6 and Fig. 7. The time resolution of the pn Fast Timing mode (0.03 ms) and Small Window mode (5.6 ms) are adequate to perform such photon phase selection. We then extracted 10 phase-resolved spectra. For the case of PSR B0656+14 this was independently done for both Fast Timing data and Small Window data. Each spectrum was then rebinned in order to have at least 40 counts per bin. Since now we are interested to study *relative* variations as a function of the pulsar phase, we didn't add systematic errors to the pn phase-resolved spectra.

As already suggested by the analysis of the energy-resolved pulse profiles, the spectra of both sources do vary as a function of the pulsars' rotational phase. This is easily seen in the first column of Fig. 9a and 9b (PSR B0656+14), Fig. 10a and 10b (PSR

B1055-52), where the observed phase-resolved spectra are compared to the best fit model describing the phase-averaged ones and the deviations are computed in units of statistical standard errors (an animated version of Figures 9a/b, 10a/b and 11a/b is available at <http://www.mi.iasf.cnr.it/~deluca/3musk/>). The variation is dramatic in the case of PSR B1055-52, owing to the high phase modulation of its emission (up to 70% in the 0.7-1.5 keV range, see Fig. 7) while it is less spectacular (but still seen with high significance) for PSR B0656+14, due to its lower modulation (pulsed fraction  $\leq 20\%$  below 2 keV, see Fig. 6). Note that in the case of PSR B0656+14 phase-resolved spectra have been rebinned in order to ease the visibility of the modulation on the graphs' scale. PSR B0656+14 and PSR B1055-52 seem therefore to share the same characteristics seen in Geminga, but their behaviours follow different trends (the case of Geminga is reported in Fig. 11a and 11b).

Turning now to the spectral fit of the phase-resolved spectra, no meaningful results could be obtained by allowing both the temperature and the normalization of the blackbodies to vary: a definite trend showing the maximum temperature in correspondence of minimum emitting area (and vice-versa) was systematically obtained in all cases. Such a modulation pattern is obviously driven by the strong correlation between the two spectral parameters, and cannot be trusted as reliable.

Thus, we have used the phase-integrated best fit model as a template to describe the phase-resolved data. The  $N_H$  value, the temperatures of both blackbodies and the power law photon index were fixed to the values best fitting the phase-integrated spectrum. The phase modulation was then reproduced by allowing the normalization parameters of each spectral component to vary independently. For the case of PSR B0656+14, spectra from Small Window data and from Fast Timing data corresponding to the same phase interval were fitted simultaneously.

As in the case of Geminga (Caraveo et al., 2004), such a simple approach (using only three free parameters) yielded a satisfactory description of the phase-resolved spectra also for PSR B0656+14 and PSR B1055-52. Reduced  $\chi^2$  of  $\sim 0.8 - 1.4$  were obtained in different phase intervals.

The results of phase-resolved spectral fits are shown in right column of Fig. 9a and 9b, Fig. 10a and 10b (the case of Geminga is represented in Fig. 11a and 11b): for each phase interval, the three best fitting spectral components are plotted, superimposed to the unfolded data points. Knowing the objects' distance values, we can then compute the emitting surface corresponding to each blackbody curve. To visualize the evolution of the spectral parameters as a function of the pulsars' phase, we have plotted the blackbody radii, as well as the power law intensities, as a function of the objects' rotational phase. This is shown in Fig. 12, Fig. 13 and Fig. 14.

The behaviour of the three neutron stars as a function of their rotational phase is vastly different. The most important results may be summarized as follows:

- The cool blackbody component shows a similar phase evolution for the three targets. The values of the blackbody radii follow a roughly sinusoidal profile with a modulation  $\leq 10\%$  (wrt. the average value) for PSR B0656+14 and for PSR B1055-52, of  $\sim 15\%$  for Geminga.
- The hot blackbody components have a similar phase evolution with a sinusoidal profile. However, we see striking differences both in the amplitude of their phase modulation and on their overall luminosity. While for PSR B0656+14 the modulation in the emitting radius wrt. the average value is  $< 10\%$ , similar to the value found for the cool blackbody component, in the case of PSR B1055-52 we see a 100% modulation, since the hot blackbody component is not seen in 4 out of 10 phase intervals. A similar, 100% modulation is observed also in the case of Geminga, although in this case the hot blackbody component is seen to disappear in just one phase interval, and the profile of its phase evolution is markedly broader. As far as the radii values are concerned, we note that they span a factor of 30, ranging from the 60 m of Geminga to the  $\sim 2$  km of PSR B0656+14.
- The study of the power law component is partially hampered, in the cases of PSR B0656+14 and PSR B1055-52, by the low signal-to-noise at energies above 1.5 keV, owing to the high background affecting the Fast Timing observations. It is therefore difficult to assess the shape of the pulse profile (single-peaked for PSR B0656+14?; double-peaked for PSR B1055-52?) and the actual modulation in such cases. Conversely, for Geminga, thanks to the different pn mode, the power law component show a clear double-peaked profile, with a significant unpulsed flux.
- The relative phase evolution of the three spectral components is vastly different for the three neutron stars. This is particularly evident when looking at the two blackbody components. In the case of PSR B0656+14 some sort of anti-correlation is observed, with the hot blackbody peaking in correspondence of the cool blackbody minimum. This is at odds with the behaviour observed for PSR B1055-52, where the two thermal components appear definitely correlated. Geminga shows an intermediate phenomenology: the cool and the hot blackbodies have a  $\sim 0.25$  difference in their phase pattern.

Of course, one could fit the phase-resolved spectra fixing the emitting radii to the average values and leaving the temperatures as free parameters. The goodness of the fits obtained following such an approach is comparable to that obtained previously fixing the temperatures

and the photon index. Not surprisingly, the evolution of the parameters, as a function of the phase, is very similar to the plots shown in Fig. 12, Fig. 13 and Fig. 14. However, such an approach renders less immediate the interpretation of the hot blackbody phase evolution especially in the case of PSR B1055-52, where the hot spot is not present for about half of the period. Maximum emitting radius translates into maximum temperature; absence of hot spot translates into  $T(\text{hot blackbody})=T(\text{cool blackbody})$ , implying important changes of temperature for the same polar cap, indeed a small portion of the neutron star surface.

## 4. Discussion

The phase-resolved spectroscopy of PSR B0656+14, PSR B1055-52 and Geminga allows for a new view of the phenomenology of these middle-aged neutron stars. While the phase-averaged spectra of our targets look very similar, their phase-resolved behaviour is quite different. This is particularly evident from Fig. 12, Fig. 13, and Fig. 14, where the evolution of the cool and hot blackbody emitting radii, as well as of the power law flux, is shown as a function of the pulsars' phase. Owing to the not optimal quality of data collected for PSR B0656+14 and PSR B1055-52 above 2 keV, here we shall concentrate on the analysis of the two thermal components, presumably coming from the star surface, albeit from different regions at different temperatures.

### 4.1. The cooler component

First, let us examine the cooler component. It is seen to come from a region encompassing a good fraction, if not the totality, of the neutron star surface as a result of the star cooling. We note that the best fitting emitting surface in the case of PSR B0656+14 is very large (observed emitting radius of  $\sim 21$  km) if compared with expectations for a standard neutron star. Distance uncertainties cannot ease the problem, owing to the very accurate radio VLBI parallax measurement (Briskin et al., 2003). In any case, a value of 15 km, corresponding to a somewhat stiff equation of state (see Lattimer & Prakash, 2001 and references therein), is marginally compatible with data (being allowed within the 99% confidence contour plot for  $N_H$  and the emitting surface shown in Fig. 2). The pulsed fraction observed in the energy range where the cooler component dominates is of 14% for PSR B0656+14 (Fig. 6), of 16% for PSR B1055-52 (Fig. 7), while for Geminga it is higher than 30% (Fig. 8).

We ascribe such a modulation to a variation of the emitting areas, going from a sizeable

fraction to the totality of the neutron star surface as a function of the rotational phase. A viable mechanism to provide some sort of phase-dependent “obscuration” of the bulk of the neutron star surface could be the magnetospheric “blanket”, originally described by Halpern & Ruderman (1993) in their study of the soft thermal emission from Geminga (see also Halpern & Wang, 1997): cyclotron resonance scattering by plasma in the magnetosphere at a few stellar radii could screen the thermally emitting surface during specific phase intervals, depending on the magnetic field configuration and viewing geometry.

Alternatively, the flux variations could also be due to large-scale surface temperature modulations, expected as a consequence of anisotropic heat transfer from the neutron star interior (Greenstein & Hartke, 1983). As discussed in Sect. 3.3, such an interpretation is consistent with the observed spectral phase variation as well. With the current data we are not able to disentangle temperature and emitting surface variation without a complete physical model. We note that the observed pulsed fraction values are much greater than expected on the basis of simple thermal models. As shown by Page et al. (1995), a few % modulation is expected in large-scale surface thermal emission, owing to the effects of gravitational bending. Pulsed fractions as high as the observed values could be explained assuming a peculiar beaming of the thermal surface emission. Owing to anisotropic radiative transfer in a magnetized plasma, an anisotropic angular emission pattern wrt the surface’s normal is indeed expected, depending on temperature and magnetic field intensity and configuration<sup>5</sup> (e.g. Zavlin & Pavlov 2002 and references therein).

## 4.2. The hot spot(s)

Turning now to the hotter component, we note that for all objects this is the most dramatically variable spectral component. It is natural to interpret such marked variations as an effect of the star rotation, which brings into view and hides one or more hot spots on the star surface. It is commonly accepted that neutron stars should have polar caps hotter than the rest of the surface. This could be due to different processes such as the bombardment of charged particles accelerated in the magnetosphere and falling back to the polar caps along magnetic field lines (return currents, see e.g. Ruderman & Sutherland 1975; Arons & Scharlemann 1979), or anisotropic heat transfer from the neutron star core, which depends strongly on the magnetic field direction and is maximum along the magnetic field lines (see e.g. Greenstein and Hartke 1983). An association of the observed rotating hot

---

<sup>5</sup>However, as noted in Sect. 3.1, current atmospheric models do not yield a satisfactory description of the spectra of the three musketeers



spot(s) with the neutron stars’ polar caps seems therefore rather obvious.

#### 4.2.1. *Luminosity and size*

The observed hot spot bolometric luminosities vary by more than 2 orders of magnitude, from the rather similar values found for PSR B0656+14 and PSR B1055-52 ( $5.7 \times 10^{31}$  erg  $s^{-1}$  and  $1.6 \times 10^{31}$  erg  $s^{-1}$ , respectively), to the much dimmer Geminga ( $1.6 \times 10^{29}$  erg  $s^{-1}$ ). The former two cases are in broad agreement with the theoretical expectations of Harding & Muslimov (2002) for polar cap heating due to downstreaming of  $e^{+/-}$  generated by curvature radiation photons. In the case of the Geminga pulsar, close to the death line for creation of  $e^{+/-}$  couples via curvature radiation, the lower polar cap luminosity is consistent with expectations for polar cap heating due to bombardment by particles created by inverse Compton scattered photons only (Harding & Muslimov, 2002; see Caraveo et al., 2004).

Straight estimates of neutron star polar cap size, based on a simple “centered” dipole magnetic field geometry (polar cap radius  $R_{PC} = R\sqrt{\frac{R\Omega}{c}}$ , where  $R$  is the neutron star radius,  $\Omega$  is the angular frequency and  $c$  is the speed of light), predict very similar radii for the three neutron stars, characterized by similar periods (233 m for PSR B0656+14, 326 m for PSR B1055-52 and 297 m for Geminga, assuming a standard neutron star radius of 10 km). The observed emitting radii are instead markedly different, with values ranging from  $\sim 50$  m for Geminga to  $\sim 2$  km for PSR B0656+14. Psaltis et al.(2000) showed that the observed polar cap radius may be different from the actual one by a large amount, due to geometrical effects. Indeed, Caraveo et al.(2004) proposed a highly inclined viewing angle to reduce the surface of the emitting region in the case of Geminga. PSR B0656+14 and PSR B1055-52 face a completely different situation, since their polar caps are significantly larger than expected. Standard estimates, based on pure geometrical considerations, are clearly unsatisfactory. Even using the unrealistically large neutron star radius found for PSR B0656+14, the inferred polar cap dimension is  $<600$  m, far less than the hot spot radius. It is also possible, as suggested by Ruderman (2003), that thermal photons be significantly reprocessed higher up in the magnetosphere, interacting with charged particles. In such a picture, the same mechanism possibly providing the bulk of the cool blackbody modulation (via the phase-dependent screening quoted in Sect. 4.1) would obviously bias all emitting radii (and temperatures) measurements based on blackbody fits.

#### 4.2.2. Modulation with phase

The observed phase modulation of the hot blackbody component is largely different for the three neutron stars both in amplitude and in pattern. In the case of PSR B1055-52 a 100% modulation is seen, the hot spot disappears for 4/10 of the pulsar period. Such phenomenology strongly argues for an oblique rotator seen at high inclination. This would favour the historical Rankin (1993) interpretation of the radio polarization pattern of this pulsar (orthogonal rotator) versus the older one (almost aligned rotator) of Lyne & Manchester (1988); however, the presence of only one visible “pole” would represent a challenge for a classical orthogonal rotator seen at high inclination. Conversely, the much lower modulation observed in the case of PSR B0656+14 seems consistent with an almost aligned rotator, with the polar cap always in sight. This picture is in good agreement with the radio pulse polarization results of Everett & Weisberg (2001), as well as with the above mentioned studies of Rankin (1993) and Lyne & Manchester (1988). The remarkably high pulsed fraction of PSR B1055-52 ( $\sim 70\%$  in the 0.7-1.5 keV range) requires a significant beaming of the hot thermal component emission. Indeed, Psaltis et al.(2000) estimated that under standard assumptions about the star mass and equation of state, pulsed fraction higher than 35% cannot be produced even in the most “optimistic” case of an orthogonal rotator having very small polar caps with a high temperature contrast wrt. the rest of the star surface. The same consideration applies to the case of Geminga (pulsed fraction of  $\sim 55\%$  in the 0.7-2 keV range, but with a significant contribution of non-thermal emission). In all cases a single peak per period is observed. This may suggest that we are seeing a single hot region on the surface of the star. The visibility of a single pole along the star rotation is consistent with the geometrical interpretation of the phase-resolved behaviour of PSR B0656+14, while for PSR B1055-5 an important role of beaming should be invoked to explain why the opposite pole emission is not seen, in spite of the effects of gravitational light bending (Zavlin et al., 1995). An alternative possibility could be a magnetic field configuration different from a standard centered dipole. In the case of a magnetic field with significant multipole components, two (or more) hot polar caps could be very close on the star surface and their emission could be blended in a single peak.

### 4.3. Phase alignment between the thermal components

Owing to the sensitivity of heat transfer to the magnetic field, a temperature anisotropy should exist on the neutron star surface, with temperature increasing towards the magnetic poles (e.g. Greenstein & Hartke, 1983). Assuming the angular distribution of the radiation emitted by a surface element to be peaked along the normal to the surface and decreasing

towards larger angles (see Harding & Muslimov 1998 and references therein), we would expect the overall emission of the neutron star to be modulated as the poles come in and out of our line of sight. In particular, maximum flux should be observed when the line of sight is best aligned with the hotter regions. If the hot spots are indeed at the magnetic poles, a definite correlation between the hotter and colder components should be clearly visible in the phase evolution of the emitting regions. While this is indeed the case for PSR B1055-52, the contrary is true for PSR B0656+14, which shows a clear anti-correlation. Geminga shows an intermediate phenomenology, with a phase difference of  $\sim 0.25$  between the hot and cool components (Fig. 14). Thus, one (or more) of the assumptions within the above simple scenario (temperature distribution resulting from a centered dipole magnetic field; pencil beaming) are not correct. Different hypotheses should be considered: the surface temperature distribution is possibly more complicated, e.g. as a consequence of a multipolar magnetic field; the hot spots may not be located close to the center of the hotter surface region; the emission beaming function may have strong peaks at angles away from the normal to the surface element. We note that magnetospheric reprocessing of thermal photons (see previous sections) could possibly ease the problem. Such a mechanism would introduce phase delays between thermal spectral components which would not be directly related to the properties of the surface, but driven by the magnetospheric structure.

The observed phase-resolved behaviour of the three musketeers does not seem to argue in favour of the simple, “canonical” picture of neutron stars as inclined, rotating, centered dipoles.

## 5. Conclusions

In general, the new X-ray phenomenology revealed by the EPIC/XMM-Newton combination presents new aspects of these three isolated, local neutron stars. Rotating, polar hot spots are clearly detected for the first time. It is tempting to link their origin to energetic particle bombardment, following the Ruderman mechanism, especially because certainly two (and possibly all) of the three musketeers are strong  $\gamma$ -ray sources. In the case of Geminga, moreover, Caraveo et al. (2003) have found a truly “smoking gun” evidence for this: the object’s bow shock is filled with electrons of just the right energy ( $\sim 10^{14}$  eV) and luminosity (a few  $10^{28}$  erg s $^{-1}$ ) to be the particles escaping from a polar cap.

However, the measurement of polar cap sizes, rendered accurate by the excellent distance measurements, does not match simple theoretical expectations. 3-D geometry, beaming physics as well as the role of magnetospheric scattering will have to be invoked for detailed models. The same holds true for the apparent sizes of the cool blackbody components. At

least in one case they exceed the expected size of a standard neutron star. Simple atmospheric models worsen the problem. However, before considering the implications of this finding on neutron stars equations of state, we must understand if the parameters of the neutron stars surfaces can be reliably derived from their thermal radiation or if some other mechanism is biasing our results.

Finally, the apparent puzzle posed by the difference in the cool and hot components phase alignments in the three objects is difficult to reconcile with existing pictures. This is reminiscent, however, of the situation at  $\gamma$ -ray energies, with different light curves. It will be very interesting to look for contemporary X-ray and  $\gamma$ -ray data when AGILE and GLAST will be in orbit with XMM-Newton.

We thank R. Manchester for his help with the Parkes radio ephemeris and A. Possenti for his useful suggestions about radio timing data. We thank A. Pellizzoni and M. Conti for their help with the EGRET data on Geminga. The XMM-Newton data analysis is supported by the Italian Space Agency (ASI). ADL acknowledges an ASI fellowship.

## REFERENCES

- Arons, J. & Scharlemann, E.T., 1979, ApJ 231, 854
- Becker, W., Weisskopf, M.C., Tennant, A.F., et al., 2004, ApJ 615, 908
- Becker, W. & Aschenbach, B.M., 2002, Proceedings of the 270. WE-Heraeus Seminar on Neutron Stars, Pulsars, and Supernova Remnants. Edited by W. Becker, H. Lesch, and J. Trümper. Garching bei München: Max-Planck-Institut für extraterrestrische Physik, p.64
- Becker, W. & Trümper, J., 1997, A&A 326, 682
- Bertsch et al., 1992, Nature 357, 306
- Bignami, G.F., Caraveo, P.A., Paul, J.A., Salotti, L., Vigroux, L., 1987, ApJ 319, 358
- Bignami, G.F., Caraveo, P.A., Lamb, R.C., 1983, ApJ 272, L9
- Briskin, W.F., Thorsett, S.E., Golden, A., Goss, W.M., 2003 ApJ 593, L89
- Burwitz, V. et al., 2004, SPIE 5165, 123
- Caraveo, P.A., et al., 2003, Science 301, 1345
- Caraveo, P.A., De Luca, A., Mereghetti, S., Pellizzoni, A., Bignami, G.F., 2004, Science, 305, 376

- Caraveo, P.A., Bignami, G.F., Mignani, R.P., Taff, L., 1996, ApJ 461, L91
- Caraveo, P.A., Bignami, G.F., Mereghetti, S., 1994 ApJ 422, L87
- Cordova, F.A., Middleditch, J., Hjellming, R.M., Mason, K.O., 1989, ApJ 345, 451
- Cheng, A.F. & Helfand, D.J., 1983, ApJ 271, 271
- De Luca, A., & Molendi, S., 2004, A&A 419, 837
- Everett, J.E. & Weisberg, J.M., 2001, ApJ 553, 341
- Fierro, J.M., et al., 1993, ApJ 413, L27
- Finley, J.P., Oegelman, H., Kiziloglu, U., 1992, ApJ 394, L21
- Greenstein, G. & Hartke, G.J., 1983, ApJ 271, 283
- Greiveldinger, C., et al., 1996, ApJ 465, L35
- Halpern, J.P. & Holt, S.S., 1992, Nature 357, 222
- Halpern, J.P. & Ruderman, M., 1993, ApJ 415, 286
- Halpern, J.P. & Wang, F.Y.-H., 1997, ApJ 477, 905
- Harding, A.K. & Muslimov, A.G., 2002, ApJ 568, 862
- Harding, A.K. & Muslimov, A.G., 1998, ApJ 500, 862
- Jackson, M.S., Halpern, J.P., Gotthelf, E.V., 2002, ApJ 538, 935
- Kern, B., Martin, C., Mazin, B., Halpern, J.P., 2003 ApJ 597, 1049
- Kirsch, M., on behalf of the EPIC calibration team, 2004, EPIC Calibration Status, Document CAL-TN-0018-2-3, available from [http://xmm.vilspa.esa.es/external/xmm\\_sw\\_cal/calib/index](http://xmm.vilspa.esa.es/external/xmm_sw_cal/calib/index)
- Kramer, M., et al., 2003, MNRAS 342, 1299
- Lattimer, J.M. & Prakash, M., 2001, ApJ 550, 426
- Lyne, A.G. & Manchester, R.N., 1988, MNRAS 234, 477
- Marshall, H.L. & Schulz, N.S., 2002, ApJ 574, 377
- Mignani, R.P., De Luca, A., Caraveo, P.A., 2004, in “Young Neutron Stars and Their Environments”, Proc. IAU Symp.218, Editors Camilo, F., Gaensler, B.M., ASP, p.391
- Mignani, R.P., Caraveo, P.A., Bignami, G.F., 1997, ApJ 474, L51
- Oegelman, H., 1995, The Lives of the Neutron Stars. Proceedings of the NATO Advanced Study Institute on the Lives of the Neutron Stars, Editors M.A. Alpar, U. Kiziloglu, J. van Paradijs; Publisher, Kluwer Academic, Dordrecht, The Netherlands, Boston, Massachusetts

- Oegelman, H. & Finley, J.P., 1993, ApJ 413, L31
- Page, D., 1995, ApJ 442, 273
- Pavlov, G.G., Zavlin, V.E., Sanwal, D., 2002, Proceedings of the 270. WE-Heraeus Seminar on Neutron Stars, Pulsars, and Supernova Remnants. Edited by W. Becker, H. Lesch, and J. Trmper. Garching bei Mnchen: Max-Planck-Institut fr extraterrestrische Physik, p.273
- Possenti, A., Mereghetti, S., Colpi, M., 1996, A&A 313, 565
- Psaltis, D., Oezel, F., DeDeo, S., 2000, ApJ 544, 390
- Ramanamurthy, P.V., Fichtel, C.E., Kniffen, D.A., Sreekumar, P., Thompson, D.J., 1996, ApJ 458, 755
- Rankin, J.M., 1993, ApJS 85, 145
- Ruderman, M. & Sutherland, P.G., 1975, ApJ 196, 51
- Ruderman, M., 2003, 4th AGILE Science Workshop, “X-ray and Gamma-ray Astrophysics of Galactic Sources”, astro-ph/0310777
- Strüder, L., et al., 2001, A&A 365, L18
- Thompson, D.J., et al., 1999, ApJ 516, 297
- Turner, M.J.L., et al., 2001, A&A 365, L27
- Zavlin, V.E. & Pavlov, G.G., 2002, Proceedings of the 270. WE-Heraeus Seminar on Neutron Stars, Pulsars, and Supernova Remnants. Edited by W. Becker, H. Lesch, and J. Trmper. Garching bei Mnchen: Max-Planck-Institut fr extraterrestrische Physik, p.263
- Zavlin, V.E., Pavlov, G.G., Shibano, Y.A., 1996, A&A 315, 141
- Zavlin, V.E., Shibano, Y.A., Pavlov, G.G., 1995, Astronomy Letters 21, 149

Table 1: Journal of XMM-Newton observations.

Pulsar/Date/Obs.Time	Camera(mode) <sup>a</sup>	Good Time	Energy	Photons(%bkg)	Count rate
PSR B0656+14	pn(SW)	5970	0.15-8.0	44600(1.7%)	7.34±0.05
2001-10-23	pn(Ti)	16850	0.15-2.0	120000(6.3%)	6.67±0.04
41.0 ksec	MOS1(FF)	37800	0.15-8.0	28100(2.1%)	0.728±0.007
PSR B1055-52	pn(Ti)	61900	0.15-6.0	84450(14.4%)	1.167±0.009
2000-12-14/15	MOS1(FF)	74000	0.15-8.0	17350(1.6%)	0.230±0.003
81.4 ksec	MOS2(FF)	74250	0.15-8.0	18700(1.6%)	0.247±0.003
Geminga	pn(SW)	55000	0.15-8.0	52850(5.4%)	0.909±0.008
2002-04-05	MOS1(FF)	76900	0.15-8.0	10170(2.2%)	0.129±0.002
103.3 ksec	MOS2(FF)	77400	0.15-8.0	11300(2.4%)	0.142±0.002

<sup>a</sup>SW: Small Window; Ti: Fast Timing; FF: Full Frame

Note. — Starting from the left, the column report (1) the target name, the date of the observation and the total time span (in ksec) of the observation; (2) the detector and its readout mode; (3) the good time (in sec) of the observation; (4) the energy range considered (in keV); (5) the overall number of counts in the source extraction region (see Sect. 2.2) and the fraction of background events in the specified energy range; (6) the background-subtracted count rate.

Table 2: Results of Timing analysis.

Pulsar	P Observed (ms)	P expected (ms)
PSR B0656+14	384.9029(2)	384.90300043(5)
PSR B1055-52	197.111812(5)	197.111809432(8)
Geminga	237.1012(1)	237.1012153(1)

---

Note. — For each target, the best period, as computed from the EPIC X-ray data, is shown (column 2) together with the value expected on the basis of the extrapolation of published ephemeris: Kern et al.(2003) for PSR B0656+14, the ATNF data pulsar archive (<http://www.atnf.csiro.au/research/pulsar/psr/archive/>) for PSR B1055-52 and Jackson et al.(2002) for Geminga. The uncertainty quoted between parentheses refers to the least significant digit.



Table 3: Results of phase-integrated spectroscopy.

	PSR B0656+14	PSR B1055-52	Geminga <sup>a</sup>
$N_H$ ( $10^{20}$ cm <sup>-2</sup> )	4.3±0.2	2.7±0.2	1.07 (fixed)
kT <sub>CBB</sub> (K)	(6.5±0.1)×10 <sup>5</sup>	(7.9±0.3)×10 <sup>5</sup>	(5.0±0.1)×10 <sup>5</sup>
R <sub>CBB</sub> (km)	20.9 <sup>+2.7</sup> <sub>-3.8</sub>	12.3 <sup>+1.5</sup> <sub>-0.7</sub>	8.6±1.0
kT <sub>HBB</sub> (K)	(1.25±0.03)×10 <sup>6</sup>	(1.79±0.06)×10 <sup>6</sup>	(1.9±0.3)×10 <sup>6</sup>
R <sub>HBB</sub> (m)	1800±150	460±60	40±10
Γ	2.1±0.3	1.7±0.1	1.7±0.1
I <sub>PL</sub> (ph cm <sup>-2</sup> s <sup>-1</sup> keV <sup>-1</sup> @ 1 keV)	4.3 <sup>+0.6</sup> <sub>-1.5</sub> × 10 <sup>-5</sup>	1.9 <sup>+0.3</sup> <sub>-0.2</sub> × 10 <sup>-5</sup>	6.7±0.7×10 <sup>-5</sup>
F <sub>0.2–8keV</sub> <sup>b</sup> (erg cm <sup>-2</sup> s <sup>-1</sup> )	1.05×10 <sup>-11</sup>	2.2×10 <sup>-12</sup>	2.3×10 <sup>-12</sup>
L <sub>PL</sub> <sup>c</sup> (erg s <sup>-1</sup> )	1.8×10 <sup>30</sup>	8.1×10 <sup>30</sup>	1.2×10 <sup>30</sup>
L <sub>CBB</sub> <sup>d</sup> (erg s <sup>-1</sup> )	5.8×10 <sup>32</sup>	4.4×10 <sup>32</sup>	3.2×10 <sup>31</sup>
L <sub>HBB</sub> <sup>e</sup> (erg s <sup>-1</sup> )	5.7×10 <sup>31</sup>	1.6×10 <sup>31</sup>	1.6×10 <sup>29</sup>
Norm <sub>pn</sub> <sup>f</sup>	Ti:1 (fixed); SW:1.05	1 (fixed)	-
Norm <sub>MOS1</sub> <sup>f</sup>	0.96	0.98	-
Norm <sub>MOS2</sub> <sup>f</sup>	-	1.07	-
χ <sup>2</sup> /dof	1.11	1.02	1.19
dof	368	327	73

<sup>a</sup>Results from Caraveo et al.(2004)

<sup>b</sup>Observed flux, 0.2-8 keV

<sup>c</sup>0.5-10 keV luminosity of power law component

<sup>d</sup>Bolometric luminosity of the Cool blackbody component

<sup>e</sup>Bolometric luminosity of the Hot blackbody component

<sup>f</sup>Normalization factor to account for calibration differences; Ti: Fast Timing mode; SW: Small Window mode

Note. — To compute luminosities we assumed a distance of 288 pc for PSR B0656+14 (Briskin et al., 2003), of 750 pc for PSR B1055-52 (Kramer et al., 2003) and of 157 pc for Geminga (Caraveo et al., 1996)

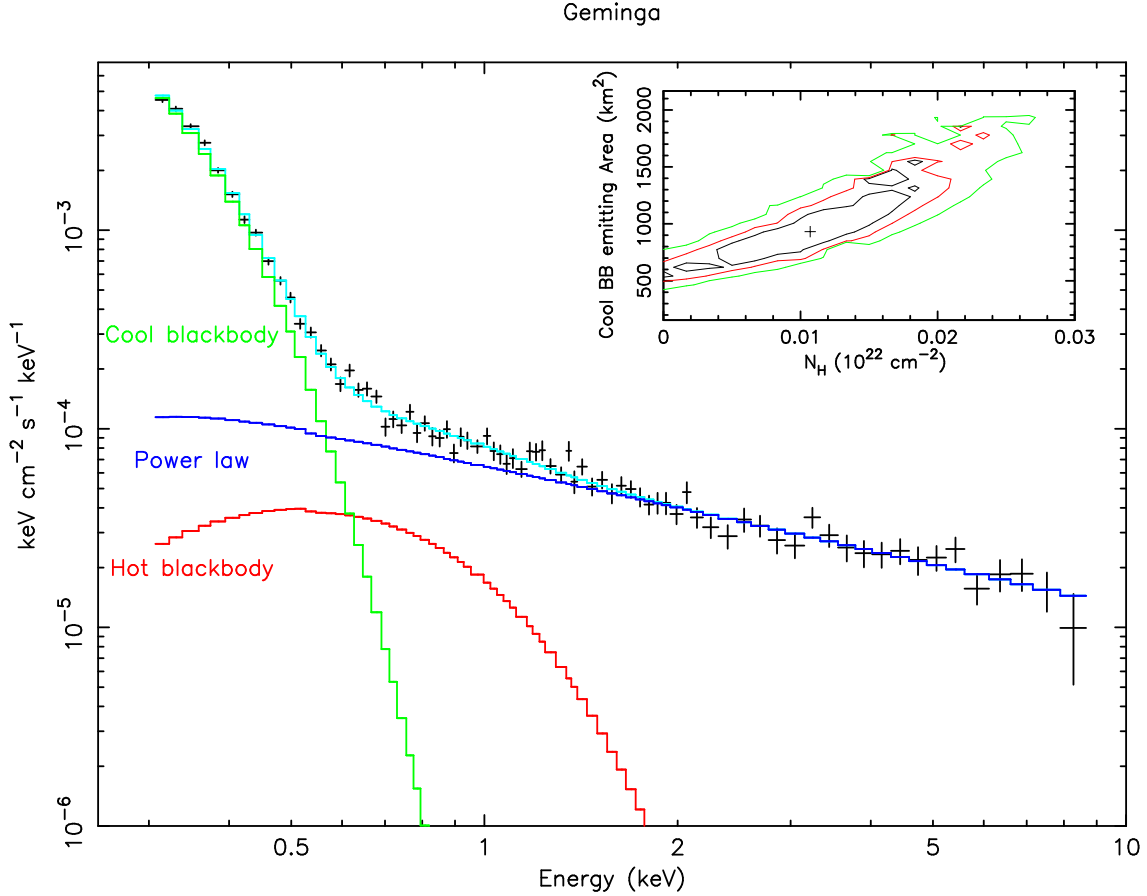


Fig. 1.— Unfolded phase-integrated spectrum of Geminga. Only data from pn camera are plotted. This figure is adapted from Caraveo et al.(2004); a different color code is used here (see also Fig. 2 and Fig. 3). The best fitting spectral model is represented by the light blue line. As discussed in the text, this is obtained by the sum of a cool blackbody component (green), a hot blackbody component (red) and a power law (blue). Detailed values of the best fitting parameters are reported in Table 3. The inset shows confidence contours for the interstellar column density  $N_H$  vs. the emitting surface for the cool blackbody. 68%, 90% and 99% confidence levels for two parameters of interest are plotted. Caraveo et al.(2004) fixed the  $N_H$  value to  $1.07 \times 10^{20} \text{ cm}^{-2}$  (resulting from ROSAT data) to obtain their set of best fitting parameters (see Table 3).

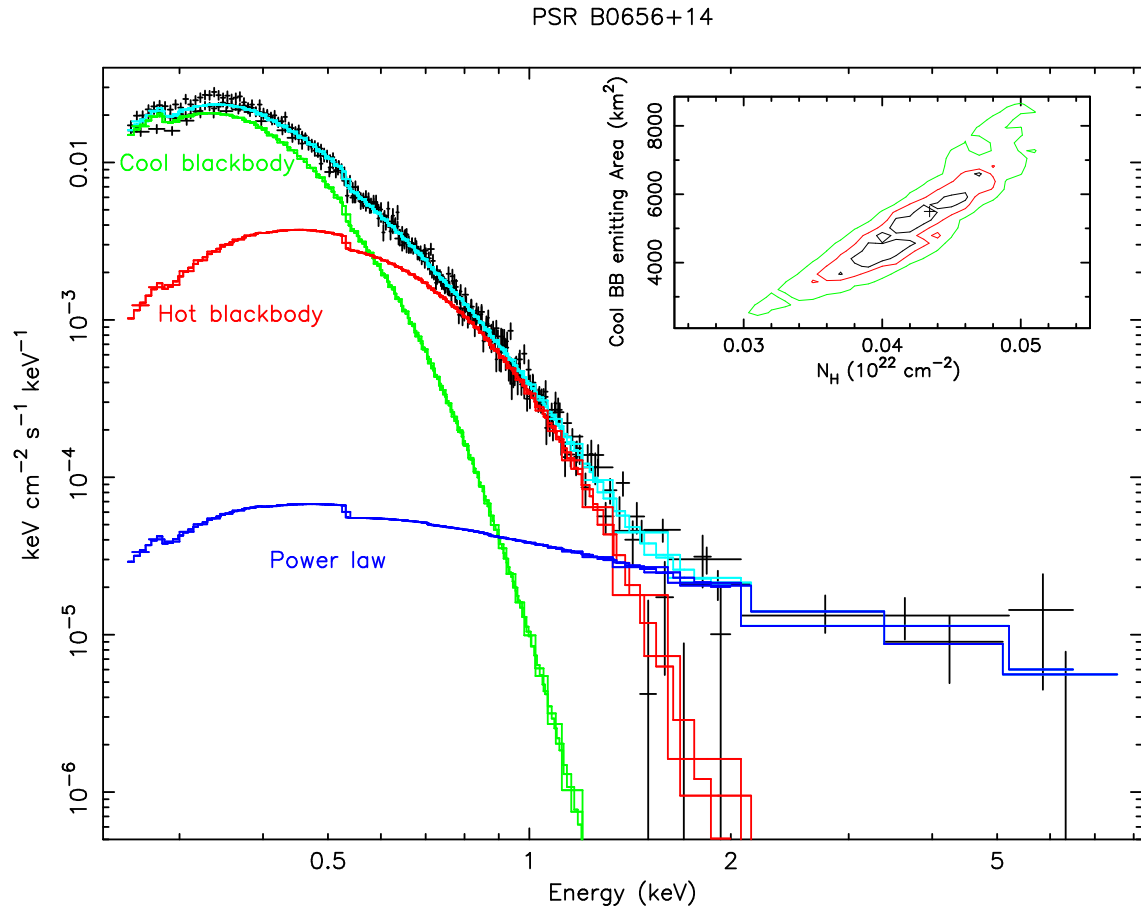


Fig. 2.— Same as Fig. 1 for the case of PSR B0656+14. Data from pn (both Small Window and Fast Timing mode) and MOS1 are plotted (black points). Detailed values of the best fitting parameters are reported in Table 3.

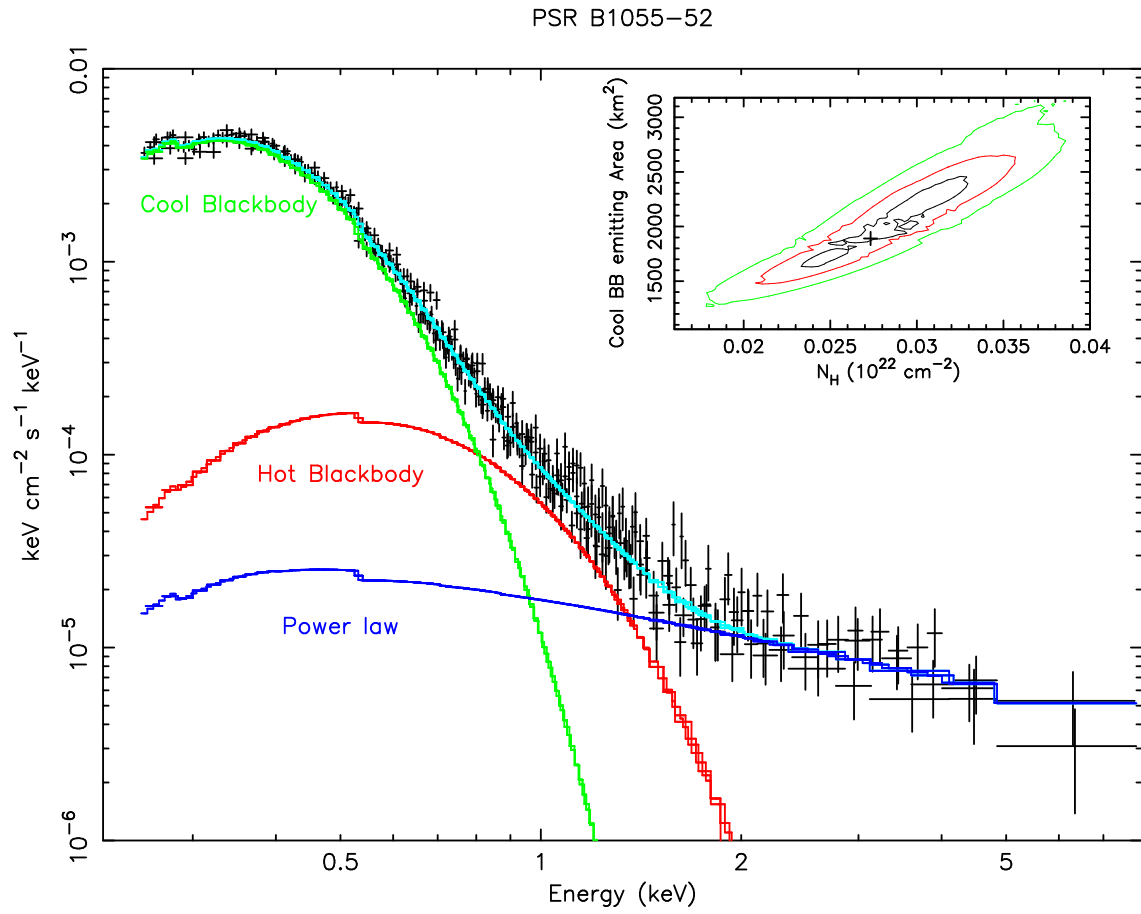


Fig. 3.— Same as Fig. 1 for the case of PSR B1055-52. Data are from pn, MOS1 and MOS2. See Table 3 for details on the best fitting spectral parameters.

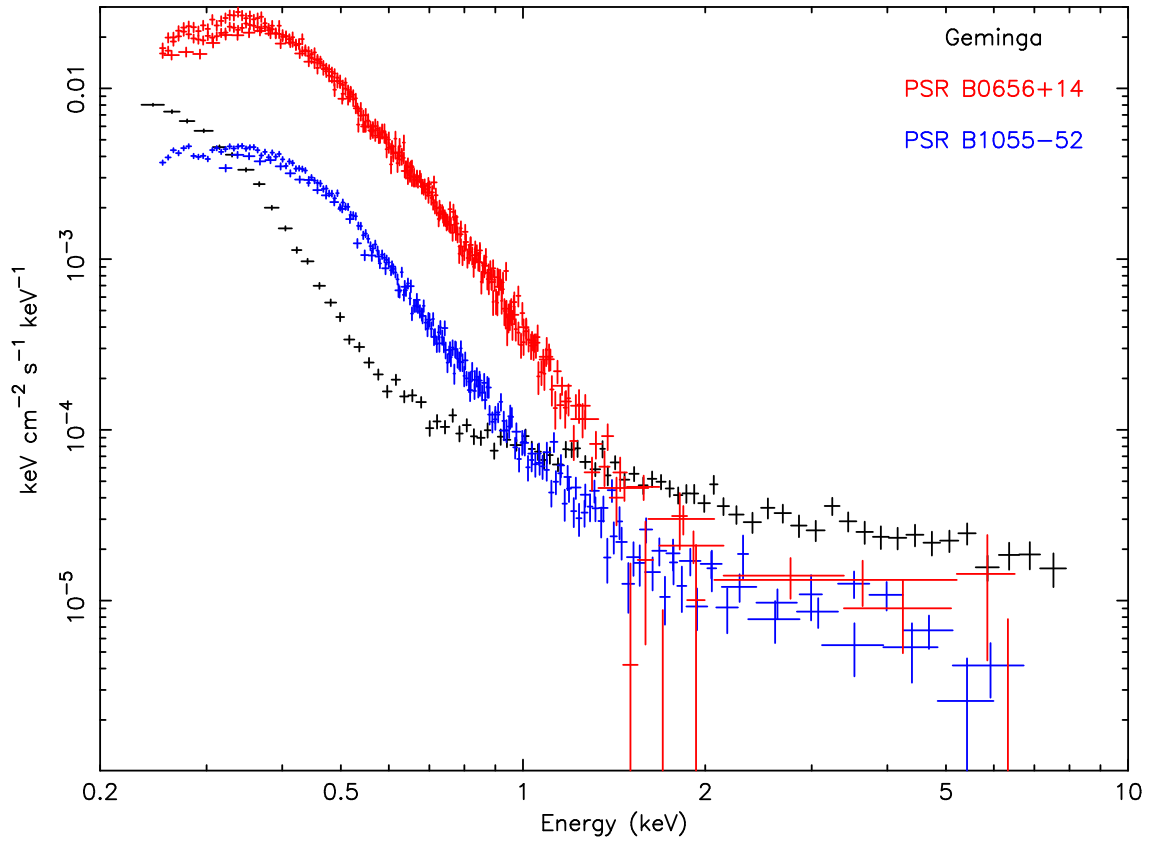


Fig. 4.— Unfolded spectra of PSR B0656+14 (red, data from pn and MOS1), PSR B1055-52 (green, data from pn, MOS1 and MOS2) and Geminga (black, data from pn). See text for details.

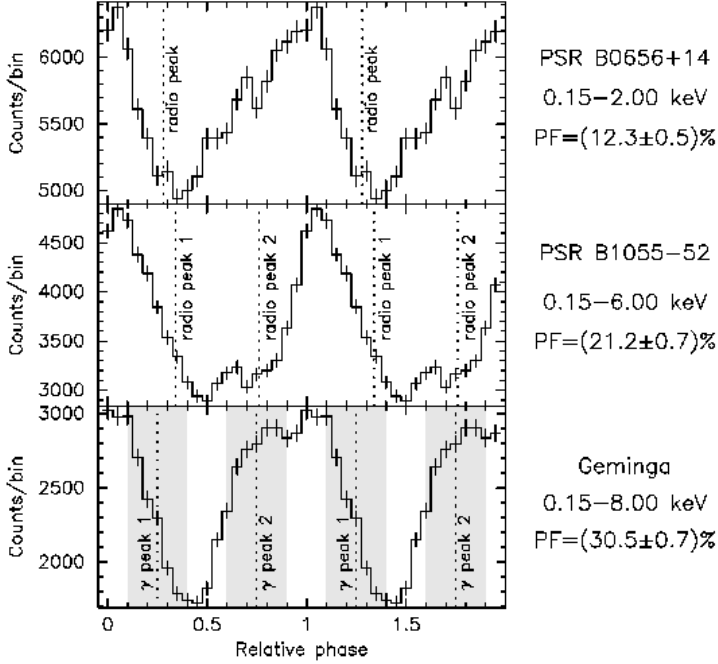


Fig. 5.— Light curves of the three musketeers. Data from pn (energy ranges: 0.15–2 keV for PSR B0656+14; **0.15–6** keV for PSR B1055–52; 0.15–8 keV for Geminga) have been folded using the radio timing solutions reported in Table 2 for PSR B0656+14 and PSR B1055–52 and the EGRET  $\gamma$ -ray ephemeris (also reported in Table 2) for Geminga. The phase has been set in order to put the X-ray maximum at phase 0. The phases of the radio peaks have been marked with vertical dashed lines; their uncertainty is estimated to be  $\sim 0.01$  (1/5 of phase bin) for the case of PSR B0656+14 and  $\sim 0.003$  ( $\sim 1/20$  of phase bin) for PSR B1055–52. See text for further details. For PSR B1055–52 “radio peak 1” refers to the highest peak in the radio profile, see also Fig. 7. We plotted also the phases of the  $\gamma$ -ray peaks for Geminga; however, as discussed by Caraveo et al.(2004), the propagation of errors in the extrapolation of the EGRET ephemeris makes their position uncertain by  $\pm 0.15$  ( such a phase interval corresponds to the gray-shaded regions; “ $\gamma$  peak 1” refers to the highest peak in the  $\gamma$ -ray profile, see also Fig. 8)

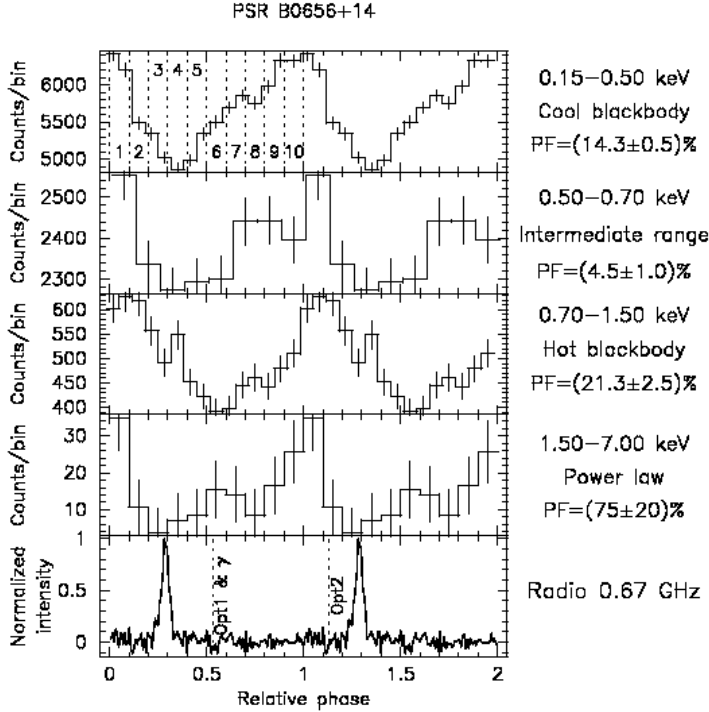


Fig. 6.— Lightcurves of PSR B0656+14 in different energy ranges. Data (obtained with pn Fast Timing mode observations, with the exception of the hardest band, based on pn Small Window mode data) have been folded using the radio ephemeris quoted in Table 2. The alignment in phase is the same chosen for Fig. 5. Although always single peaked, the pulse profile changes significantly going from the softest energy range (dominated by the cool blackbody) to the 0.7-1.5 keV range (dominated by the hot blackbody). Note the minimum in the pulsed fraction in the intermediate 0.5-0.7 keV range. Above 1.5 keV the lack of statistic hampers a detailed study of the pulse profile. The radio light curve is shown in the lower panel. The uncertainty on the phase alignment of the X-ray light curve with the radio one is of  $\sim 0.01$ . The single radio pulse is seen to trail the X-ray maximum by  $\sim 0.2$  in phase. The phases of the two optical peaks (Kern et al., 2003) as well as of the  $\gamma$ -ray peak claimed by Ramanamurthy et al.(1996) are also shown. See text for further details.

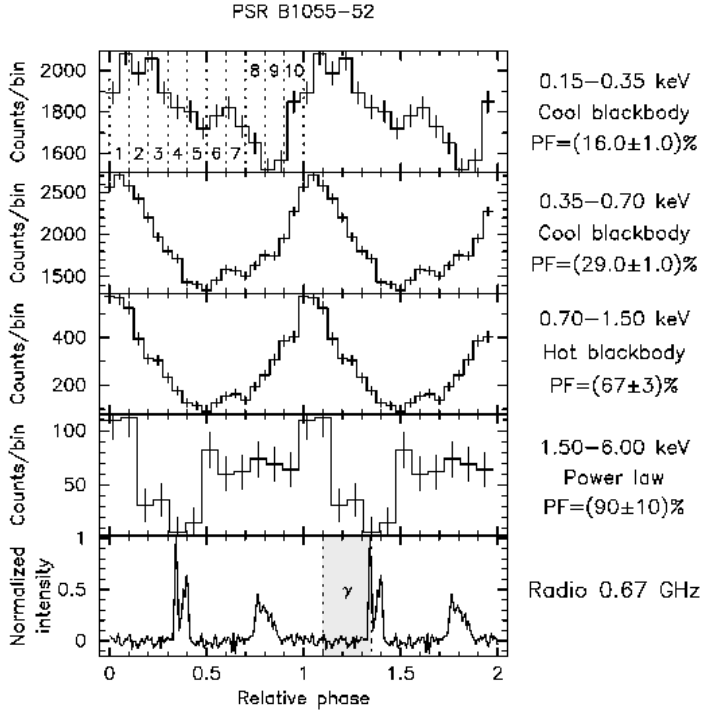


Fig. 7.— Light curves of PSR B1055-52. Note the broader profile of the X-ray pulse below 0.35 keV and the small ( $\sim 0.1$ ) phase shift wrt. higher energies. Note the value of the pulsed fraction, which grows with energy and is remarkably high ( $\sim 70\%$ ) in the 0.7-1.5 keV range, where the neutron star emission is dominated by the hot blackbody component. For a more detailed study of the energy resolved pulsed fractions see Becker & Aschenbach (2002). Above 1.5 keV the low signal-to-noise hampers a detailed study of the pulse profile. We plotted in the lower panel the radio light curve. The uncertainty on the phase alignment is of  $\sim 0.003$ . The two radio peaks are observed to bracket the single X-ray peak. The  $\gamma$ -ray pulse (Thompson et al., 1999) occurs in the gray-shaded phase interval between the two vertical dashed lines.



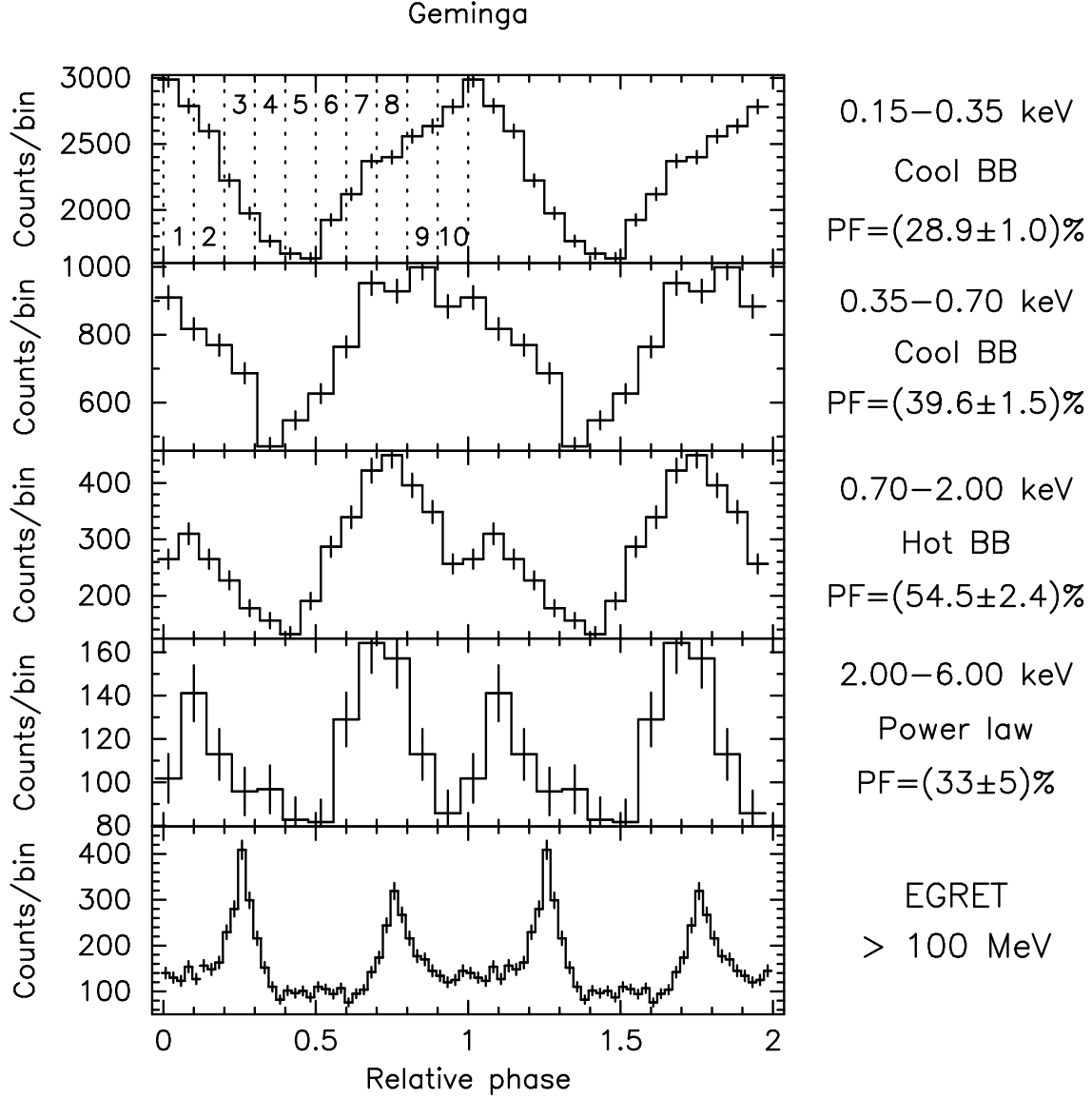


Fig. 8.— Light curves of Geminga. As discussed by Caraveo et al.(2004), the pulse shape changes as a function of energy. The single, broad peak observed at low energy (where emission from the cool blackbody dominates) changes to two peaks at higher energies (where the power law component dominates). The pulsed fraction is maximum in the 0.7-2 keV range, where the hot blackbody component is more important. The lower panel show the EGRET  $\gamma$ -ray lightcurve. The extrapolation of the  $\gamma$ -ray ephemeris makes the absolute phase alignment uncertain by  $\pm 0.15$ , owing to the long time span between the EGRET and the EPIC observations. Note that the numbering of the phase intervals defined in the upper panel is different from that used by Caraveo et al. (2004). Their phase 1 is here phase 3 and similarly for all.

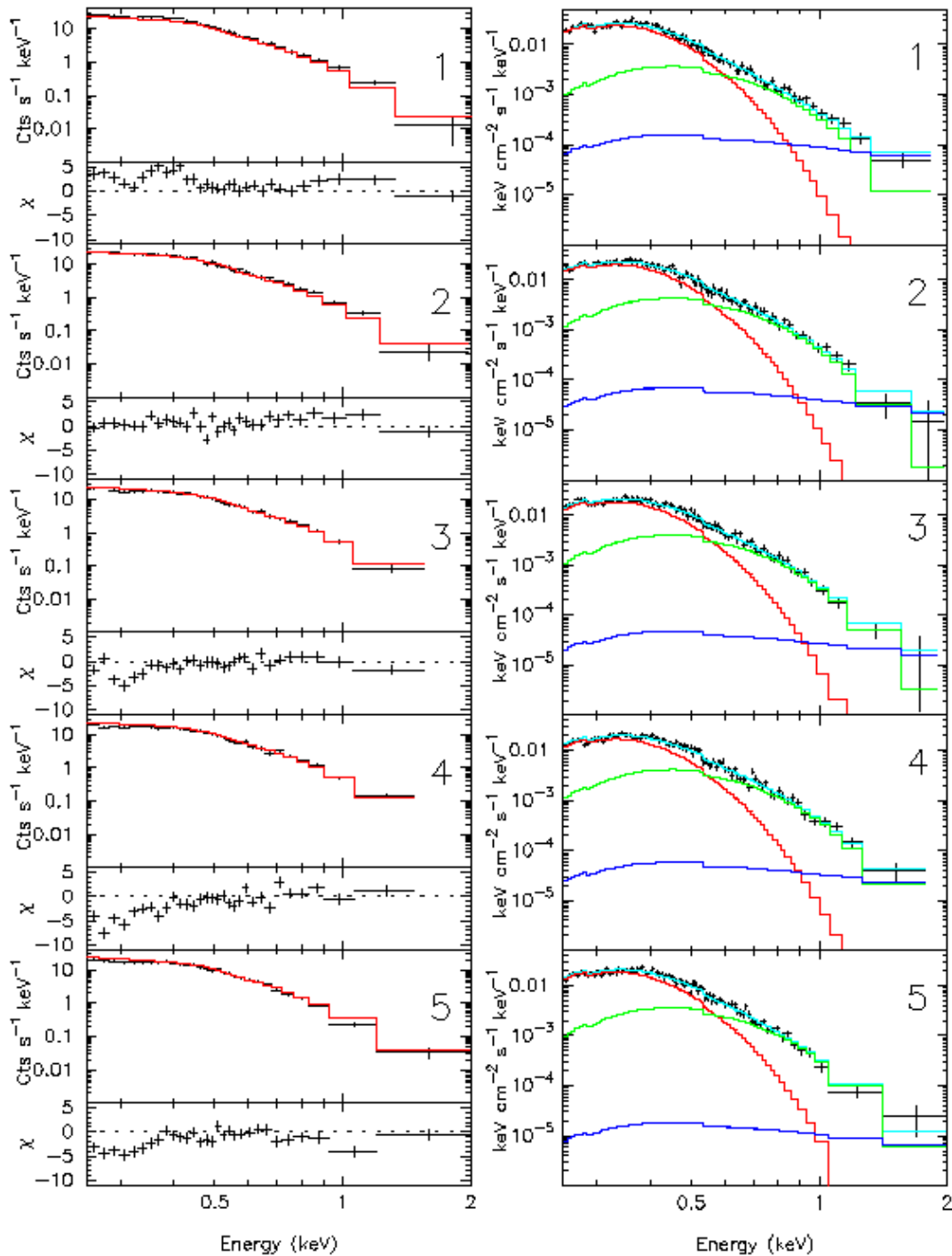


Fig. 9a.— Phase-resolved spectra of PSR B0656+14. Photons have been selected in correspondence of the phase intervals marked in Fig. 6. Phase intervals from 1 to 5 are shown here; phase intervals 6-10 are shown in Fig. 9b. Upper panels on the left column present, for each phase interval, the observed spectrum (data points) compared to the best fit model (solid line) of the phase-integrated spectrum (upper plots); lower panels show the difference between data and such model in units of statistical errors. To ease the visibility of the deviations of phase-resolved spectra from the averaged spectrum template, spectral channels have been rebinned. Panels on the right column show, for each phase interval, the unfolded spectrum together with its best fit model. The model components are also plotted (color code as in Fig. 2). An animated version of Figures 9a/b, 10a/b and 11a/b is available at <http://www.mi.iasf.cnr.it/~deluca/3musk/>

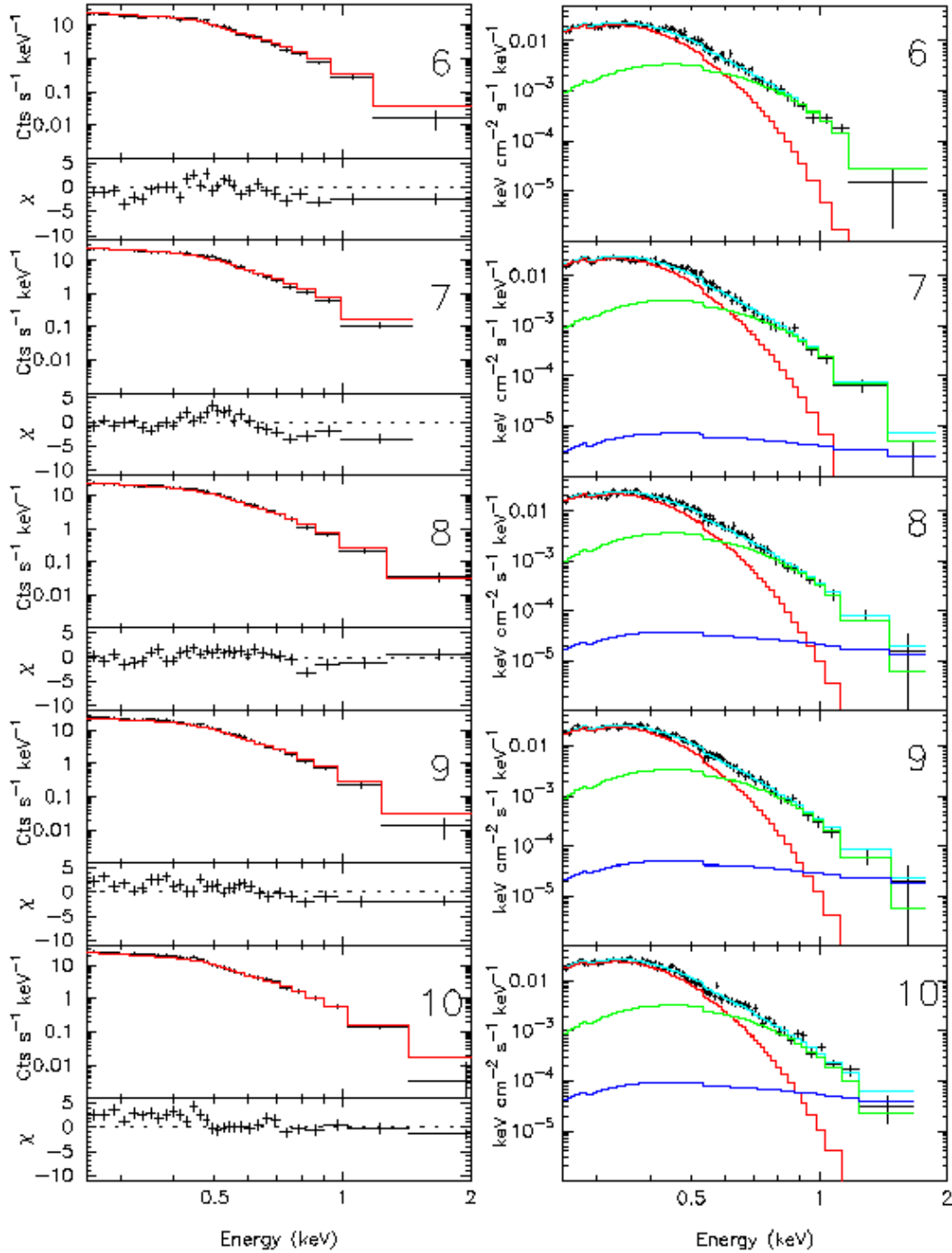


Fig. 9b.— Phase-resolved spectra of PSR B0656+14. Same as Fig. 9a, phase intervals 6-10 are shown.

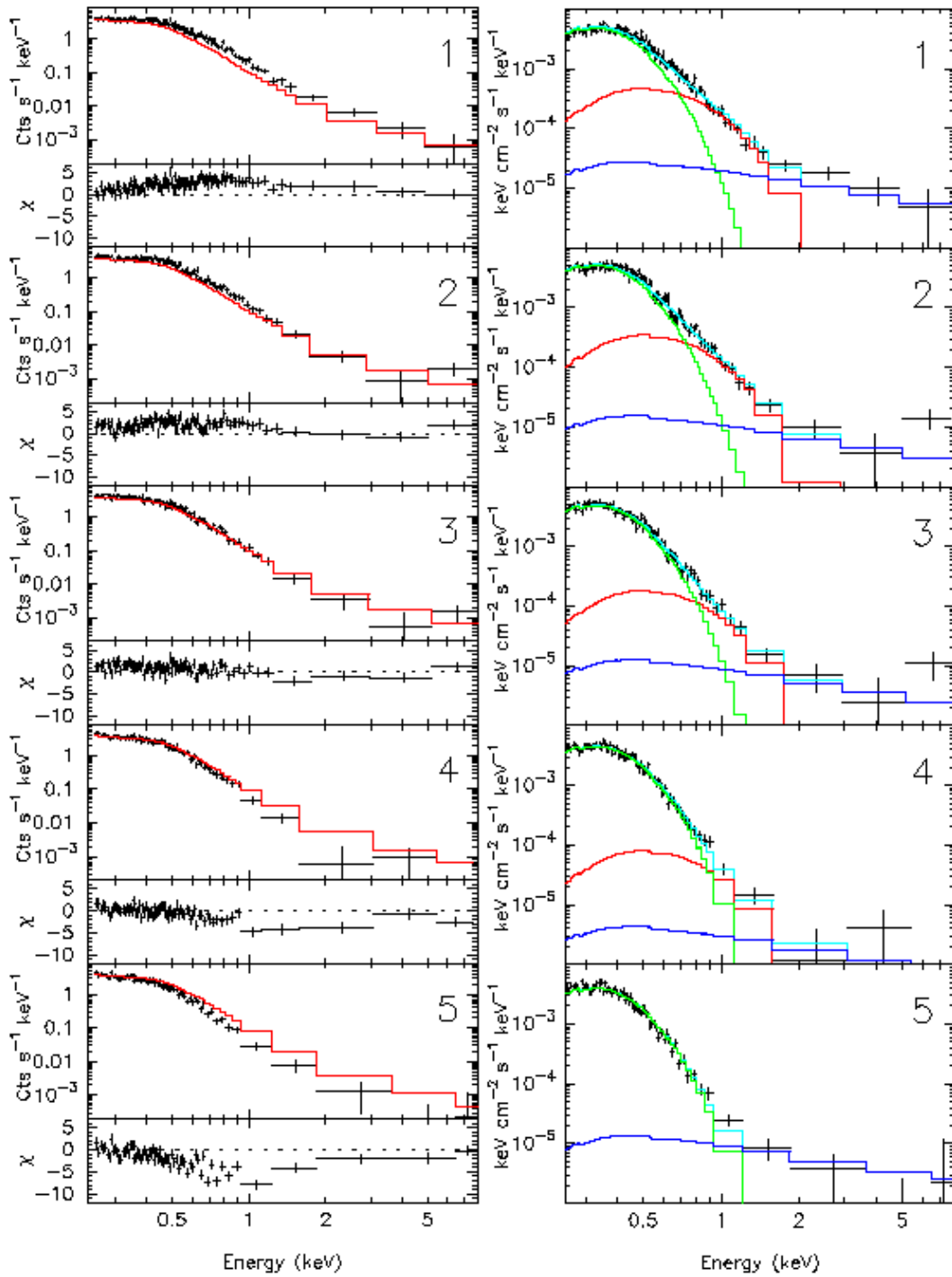


Fig. 10a.— Phase-resolved spectra of PSR B1055-52. Phase intervals 1-5 (according to the notation of Fig. 7) are displayed. See caption to Fig. 9a for explanations. Data have not been rebinned. Note the much higher deviations of the phase-resolved spectra wrt. the average one.

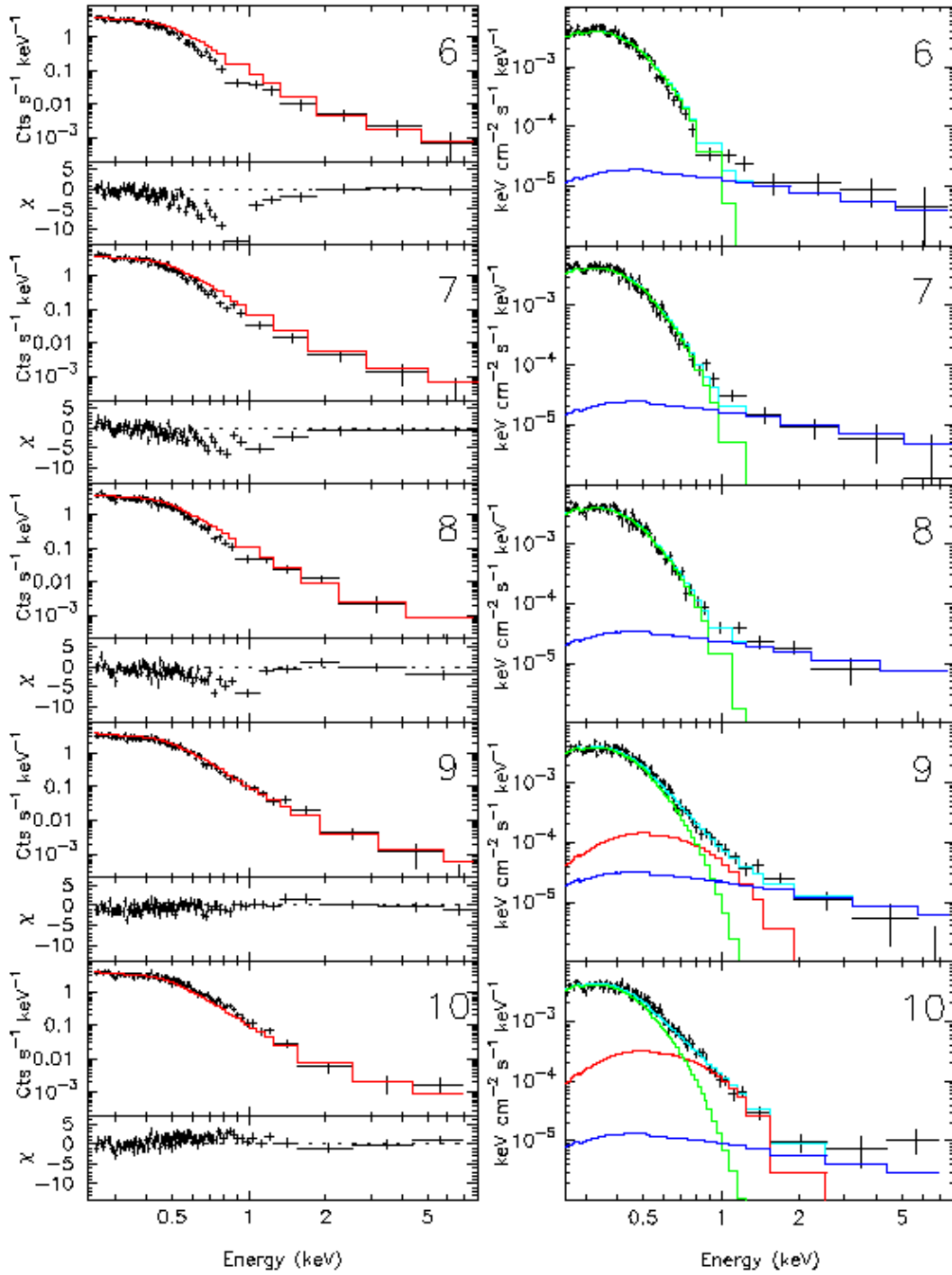


Fig. 10b.— Same as Fig. 10a, phase intervals 6-10 are shown.

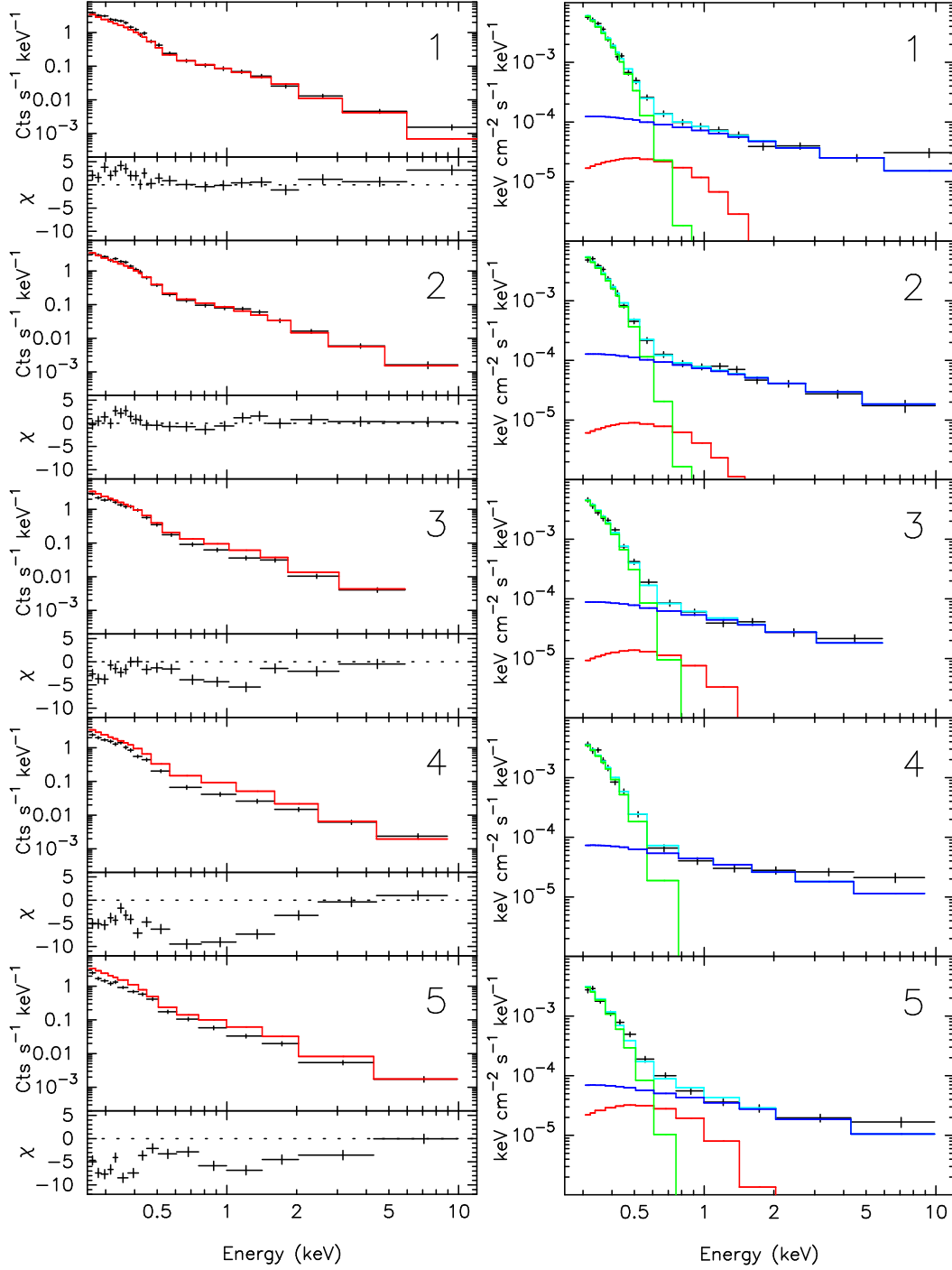


Fig. 11a.— Phase-resolved spectra of Geminga. Phase intervals 1-5 (see Fig. 8) are shown here. See caption to Fig. 9a for explanations. The figure is adapted from Caraveo et al.(2004), according to the phase numbering and color code adopted in this work.

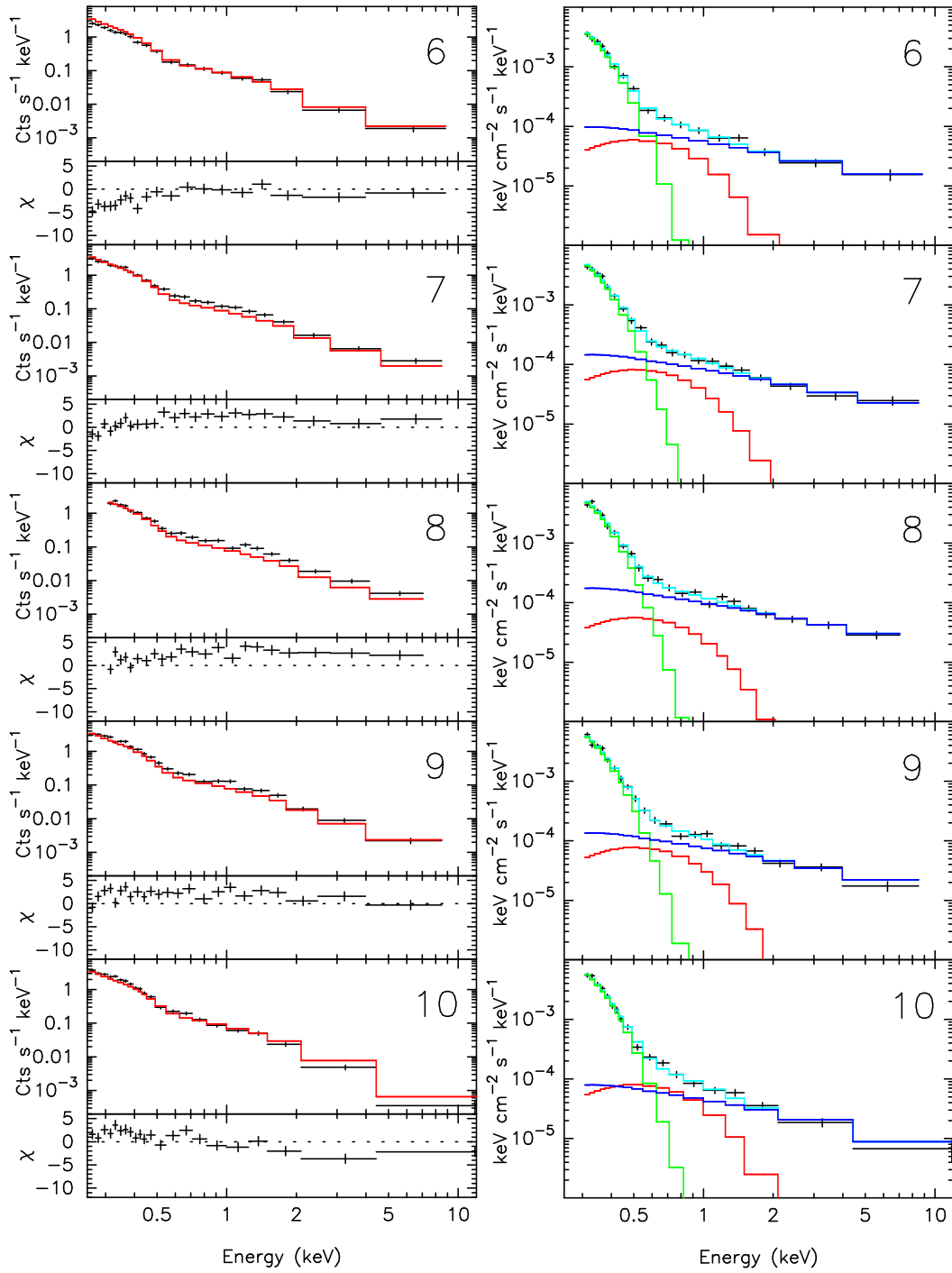


Fig. 11b.— Same as Fig. 11a, phase intervals 6-10 are displayed.

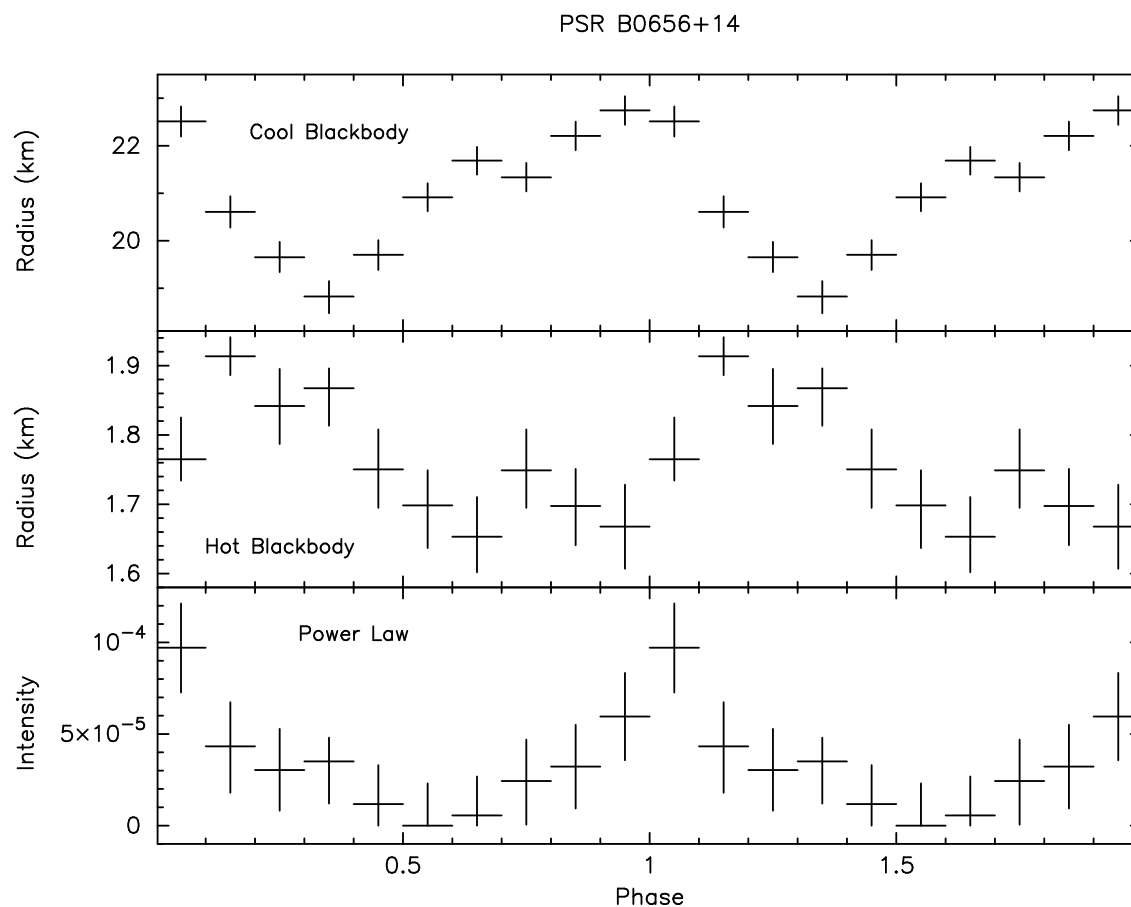


Fig. 12.— The parameters best fitting the phase-resolved spectra of PSR B0656+14 are plotted as a function of the pulsar phase defined as in Fig. 5. Both cool and hot blackbody emitting surfaces evolve throughout the pulsar phase following a sinusoidal pattern showing an overall  $\sim 10\%$  modulation (wrt. the average values) on the emitting radii value. Note the marked anti-correlation between panel 1 and panel 2 with the hot blackbody peaking in correspondence of the cool blackbody minimum. The power law component has a different phase trend wrt. the thermal components, with a single, sharper peak.



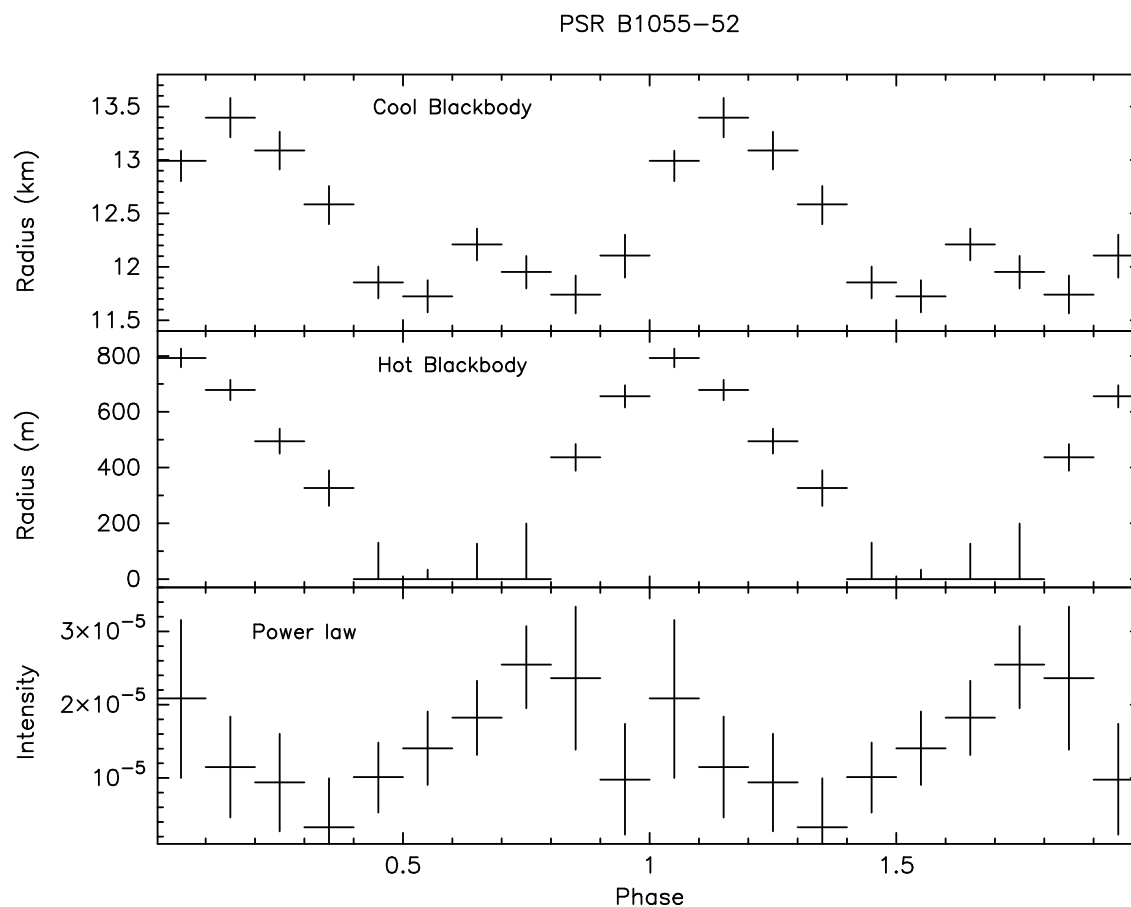


Fig. 13.— Same as Fig.12, for PSR B1055-52. While the cool blackbody emitting radius shows a  $<10\%$  modulation (wrt. the average value), the hot blackbody component show a dramatic,  $100\%$  modulation since its contribution is null in 4 of the 10 phase intervals. Note that for PSR B1055-52 the two thermal components have a similar time evolution, with a phase shift as low as  $\sim 0.1$ . The power law component has a different modulation; it is difficult to assess whether its profile is single-peaked or double-peaked, owing to the lower signal to noise in the high energy portion of the spectra.

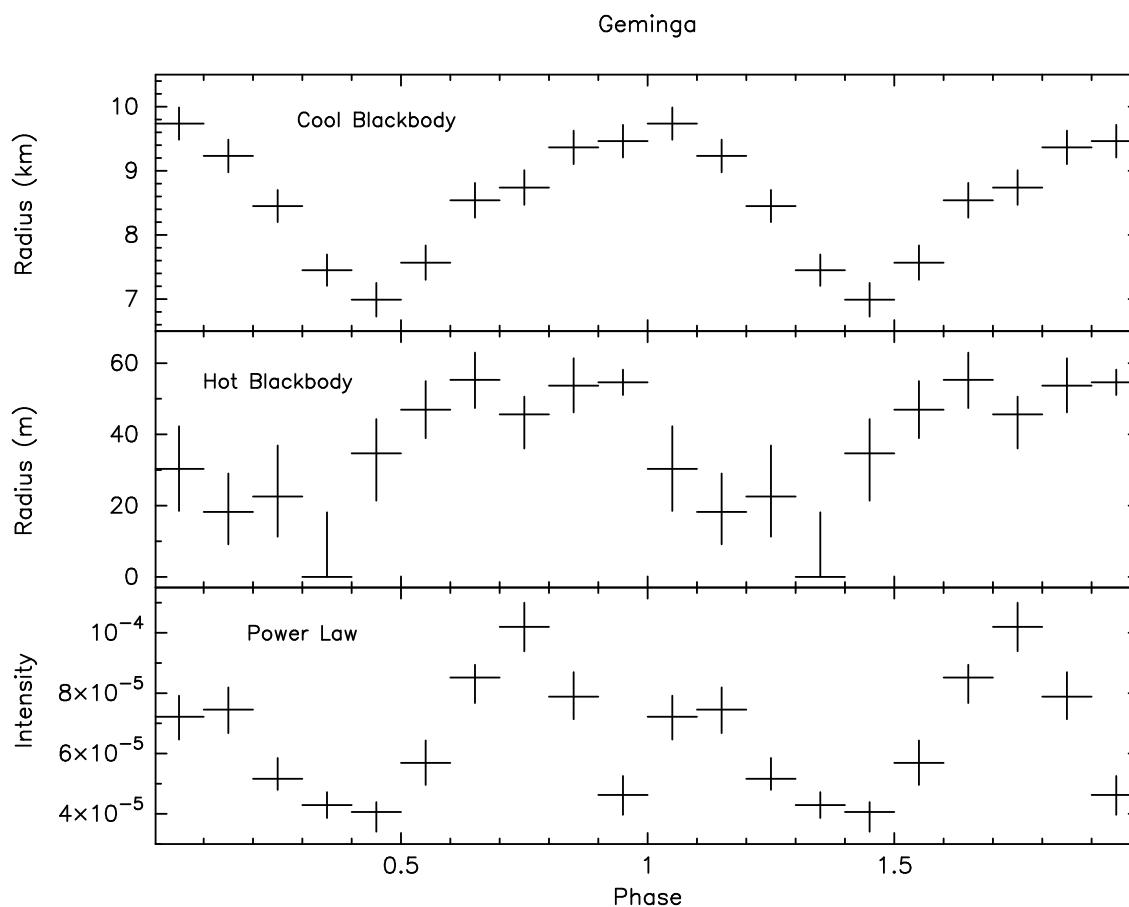


Fig. 14.— Same as Fig.12 and Fig.13 for the case of Geminga. The figure is adapted from Caraveo et al.(2004) (see their Figure 4), according to the choice of phase adopted in this work. The cool blackbody component shows a  $\sim 15\%$  modulation (wrt. the average value) of its emitting radius, with a sinusoidal profile. Conversely, the hot blackbody is 100% modulated, and disappears for 1/10 of the pulsar period. The power law component has a remarkably different, double-peaked phase profile and shows a significant unpulsed fraction.